# Designing oscillating cilia for regulating particle motion in microfluidic devices

A Thesis
Presented to
The Academic Faculty
by

Rajat Ghosh

In Partial Fulfillment
of the Requirements for the Degree of Master of Science in
The George W. Woodruff School of Mechanical Engineering

Georgia Institute of Technology
May 2010

# Designing oscillating cilia for regulating particle motion in microfluidic devices

Approved by:

Dr. Alexander Alexeev, Advisor
Woodruff School of Mechanical Engineering
*Georgia Institute of Technology*

Dr. Minami Yoda
Woodruff School of Mechanical Engineering
*Georgia Institute of Technology*

Dr. David Hu
Woodruff School of Mechanical Engineering
*Georgia Institute of Technology*

Date Approved: April 1, 2010

*This work is dedicated to the almighty God and her beautiful nature. I wish to know how the nature works, and aspire to utilize her energy for the benefits of mankind. Exploring her mysteries in the context of technological advancement has been my greatest motivation.*

## ACKNOWLEDGEMENTS

In the present research work, I was extremely fortunate to be advised by Dr. Alexander Alexeev at Georgia Tech. From his vast academic experience in fluid mechanics, he has guided my research as a Master's student. By working with him, I have got a valuable exposure in advanced fluid mechanics research and developed an ability to tackle a fluid mechanics problem in a systematic manner. I am deeply indebted to his contribution in this scholastic work. I would also like to express my gratitude to Dr. Minami Yoda and Dr. David Hu for spending their valuable time as my committee member. I have immensely benefited from their advices on my thesis. I appreciate their assistance, and technical insight. I would also like to thank my lab-mates – Hassan Masoud, Wenbin Mao, and Alex Kilimnik for their sincere support and encouragement. Hassan and Wenbin, as senior students, guided me in numerous occasions.

My research was partially funded through teaching assistantship I received from G.W. Woodruff School of Mechanical Engineering, Georgia Tech. In this regard, I am very thankful to Dr. Wayne Whiteman, Dr. Levant Degertekin, Dr. Williams E. Singhose, and Dr. J. Rhett Mayor for their supervision. I would also mention my fellow teaching assistants, Alex Williams, Daichi Fujioka, Mark Varady and others for their support. I would also appreciate the efforts from Ms. Glenda Johnson for her constant administrative assistance.

I must also pay homage to all course instructors at Georgia Tech, IIT Kharagpur, my Schools and different tutors for their dedicated effort and time for educating me with study and research skills of different levels. It is their patient training that shapes my intellectual personality. Last but not the least; I am extremely thankful to my parents and sister for their constant encouragement and support. Without their trust, I would never get this education.

LIST OF CONTENTS

## LIST OF TABLES

## LIST OF FIGURES

## SUMMARY

We design actuated cilia that can maneuver microscopic particles normal to a microfluidic channel wall and transport microscopic particles parallel to the channel wall. For identifying the design specifications, we employ a hybrid LBM/LSM computational model, to simulate hydrodynamic interactions between oscillating elastic cilia and microscopic particles in a microfluidic channel. The oscillating synthetic cilia are elastic filaments tethered to the channel wall and actuated by sinusoidal force acting at their free ends. The cilia are arranged in a square pattern. The microscopic particle is a neutrally buoyant solid sphere, which is sufficiently small compared to the cilium length and inter-cilium distances, so that the particle can move freely inside the ciliated layer.

We study the effect of actuation frequency on the particle motion inside the ciliated layer. We show that depending on the frequency, particles can be either driven away from the ciliated channel wall or drawn towards the wall. We also examine how to use inclined cilia to transport particles along the ciliated layer. We show that the particle transport along the ciliated layer can be regulated by the frequency of cilium oscillation. The results uncover a new route for regulating particle position and transport in microfluidic devices.

# CHAPTER 1

# INTRODUCTION

There is currently great interest in combining the functional components that are necessary for performing complex chemical and bio-chemical analysis into micron-size integrated devices. The potential miniaturized integrated devices could have a number of technical capabilities: the ability to use very small quantities of samples, and reagents and to carry out separations and detections with high resolution and sensitivity; low cost; short times for analysis; and small footprints for the analytical devices [1-2]. This integrated unit has been described as micro total analysis system (μTAS) or Lab-on-a-chip devices [3-6]. It offers fundamentally new capabilities in the control of concentrations of molecules in space and time and therefore, these devices have potential to be of great importance in genomics, drug screening, and clinical applications.

Microfluidics, i.e., the control of flow of small volumes (from $fL$ to $\mu L$) of liquids in microscopic (1-1000 $\mu$m) channels, is the central technology in this field. Microfabricated integrated circuits [7] revolutionized computation by vastly reducing space, labor and time required for calculation. Microfluidic systems offer similar promise for large-scale automation of chemistry and biology [5], suggesting numerous experiments being performed in parallel. The increasing availability of microfluidic systems of various geometries and materials for the downscaling of chemical or biochemical processes raises a strong demand for adequate techniques to precisely determine flow parameters and to control fluid and particle manipulation. Particle control in microfluidic channel poses an important problem, considering numerous biological applications involve navigating microscopic solid particles in microflows. Traditional particle transport by turbulence is not feasible in micro-flow characterized by low Re. For microflows, with higher surface area-to-volume ratio, inertia of particles become negligible

compared to enhanced viscous drag. Thus, traditional particle control methods, which rely on inertia, would not be effective in this length scale.

### 1.1. Driving Mechanisms in Microfluidic Devices

Driving surrounding fluid in microchannel is an essential requirement for propelling particles through micro-channel. Proximity of boundaries, owing to small size of micro-fluidic devices, posits strong influence of channel boundary effect in associated microflows. Expectedly, the driving techniques that exploit the boundary effects are quite effective in microfluidic manipulation. Based on driving agents and their interactions with channel boundary, transport mechanisms in the context of microfluidic devices can be classified as being either mechanical or non-mechanical.

Mechanical pumping systems are typically based upon the deflection of a thin membrane into a pumping chamber or channel. The deflected membrane forces the liquid through the channels to create a pumping action. Membrane actuation in these systems can be done electrostatically [8], piezoelectrically, or thermoneumatically [9-11]. By using multiple membrane chambers, a peristaltic pumping action can be achieved [12]. Alternatively, a reciprocating type pump can be constructed by combining two check valves with a single membrane actuator. These mechanical systems are designed for operating on continuous liquid streams; consequently, they may be well suited for simple continuous monitoring applications such as in liquid chromatography.

Nonmechanical pumping involves application of body-force on fluid. Since Bart et al. have devised micro-electrohyrdodynamic pump [13], several methods for controlling the flow of liquids in microfluidic systems have been reported [14-15], and electrokinetic control in microfabricated capillaries has received the most attention [16]. Electrokinetic control has

several features that make it an attractive option for miniaturized systems: (i) pumping of fluids in the channels, which arises from electroosmotic flow (EOF) in capillaries with charged walls, and the control of the direction of flow are easy to implement and require only a computer-controlled high-voltage (1-30 $kV$) power supply, electrodes, and a series of relays; (ii) in electrophoretic mode, electrokinetic control results in separations of molecules by size and charge and can be used for chemical analysis; (iii) the microscopic (<100 $\mu m$) channels required to generate EOF can be defined in a number of materials, e.g., glass, quartz, and polymers, using microfabrication. Electrokinetic pumping has some serious disadvantages as a method of controlling the flow of fluids, however. First, it is sensitive to the physicochemical properties, such as ionic strength and pH, of the fluid being pumped. For example, liquids with high ionic strength cannot be pumped using EOF due to excessive Joule heating; it is, therefore, difficult or impossible to pump biological fluids, such as blood and urine, by this method. Second, the high-voltage power supplies used have adverse safety implications and power and space requirements. Third, because electrokinetic pumping requires continuity in the fluid in the channels, it does not work in the presence of trapped bubbles (e.g., air), and care has to be taken to ensure that the channels are free of bubbles. Finally, and most importantly, although EOF is well suited to controlling small volumes of liquids in narrow (<100 $\mu m$ ) channels, it cannot be used to pump liquids at high flow rates (>1 $\mu L/s$) in wider channel capability that is needed for some microfluidic applications, e.g., sample preparations because of Joule heating.

Magnetohydrodynamics presents another mechanism for driving liquid and particles in microfluidic devices.Jang et al. [17] developed a micropump based upon magnetohydrodynamics (MHD) principles. Since in many microfluidic applications, one uses buffers and solutions that are electrically conductive, one can transmit electric currents through the solutions. In presence

of an external magnetic field, the interaction between the electric currents and magnetic fields results in Lorentz body forces, which, in turn, can be used to propel and manipulate fluids. Trapping and transport of single cells are being investigated and recently, advances have been made towards the detection of magnetic material on-chip. Magnetic particles can be transported with time-varying electromagnetic fields, along patterned metallic surfaces.[18] The advantage of MHD compared to electrokinetics is operation at relatively small electrode potentials, typically below 1 V, and much higher flow rates as long as the conduit's dimensions are not too small. The disadvantage of MHD is that it is a volumetric body force which scales unfavorably as the conduit's dimensions are reduced. Xiang et al. [19] further improved the MHD idea by introducing appropriate patterning of the electrodes.

Using a rotating disc [20], variable flow rates , ranging from less than 10 nl $s^{-1}$ to greater than 100 µl $s^{-1}$ , can be achieved depending on disc geometry, rotational rate (RPM), and fluid properties. Duffey et al. [21] developed a centrifugal force based particle driving mechanism. Centrifugal effect in a rotating microchannel, is insensitive to physicochemical properties such as pH, ionic strength, or chemical composition (in contrast to AC and DC electrokinetic pumping). Aqueous solutions, solvents (e.g., DMSO), surfactants, and biological fluids (e.g., blood, milk, urine) have all been pumped successfully. This approach of fluid pumping facilitates valving action. In traditional pumps, two one-way valves form a barrier for both liquids and particles. In the case of the microcentrifuge, valving is accomplished by varying rotation speed and capillary diameter.

Few inertial phenomena such as acoustic streaming can play significant role in micro flow control. High frequency acoustic wave can circumvent difficulties associated with small scales. Even though it is periodic, due to inertial non-linearity, it can rectify oscillatory fluid

motion to give time-averaged flow referred as steady or acoustic streaming [22]. A manifestation of acoustic streaming is quartz wind [23]**.** The quartz wind is employed for driving microflow, by sending acoustic wave along a channel, with the length of $L \geq \alpha^{-1}(\omega)$, where $\alpha^{-1}(\omega)$ is the attenuation length of the acoustic wave. Non-linear inertial effect permits rectification forcing and gives rise to steady body force leading to a Poiseuille flow with a flow rate $\sim \rho U_0^2 \omega^4 / \mu L$. In quartz wind, streaming, arising within a fluctuating flow field, is commonly associated with attenuation due to viscosity. While quartz wind based streaming occurs in the bulk of the liquid, steady streaming flows occur around solid boundaries. Solid boundary with oscillatory flow gives rise to steady boundary-driven streaming [24] with time-averaged velocity $\sim U_0^2 /(\omega R)$. Examples that might find uses in mixing and pumping in microfluidic application include streaming due to oscillatory flow in curved pipes [25], tapering channels [26], and channels with variable cross-section [27].

### 1.2. Bio-inspired Micropumping

Creating non-zero time-averaged flow in a typical biological system is challenging because of large viscous damping. The situation can be compared to swimming at a low-Re flow. Similar to microfluidic devices, fluidic environment of biological systems is typically characterized by sub-millimeter length scales and a low Re hydrodynamics. Biological systems such as paramecium use cilia for pumping fluid. Cilia are a short hair-like structures (approximately $10\mu m$ in length), present on surfaces of many cells, notably in some protozoans and some type of vertebrate epithelium [28]. Cilia usually occur in large groups and are functionally and structurally similar to eukaryotic flagella. They exhibit beating motion induced by the molecular motors embedded in the cell membrane. Beating cycle of cilia consists of a fast power stroke and a slow reverse stroke [29] . Beating cilia can produce cell movement or current in the fluid surrounding them.

Typical range of beating frequency of biological cilia is $10-100Hz$ and cell propulsion velocity is of the order $10mm/\min$. In human lung, cilia are responsible for keeping it clean from foreign dust particles and bacteria. Marine animals use cilia for trapping food particles from their environment. Paramecium, a group of uniceller ciliated protozoa, utilizes beating motion of cilia for locomotion and food gathering [30].

As highlighted by Riisgard et al. [31], ciliary sieving and ciliary collecting are prevalent particle extraction mechanism employed by invertebrate marine microorganisms. Examples of such arrays are found in bivalves, ascidians, brachiopods, bryozoans, phoronids, polychaetes and larval echinoderms. These motile, microscopic cilia experience the surrounding medium as a low Reynolds number fluid [32], i.e., a highly viscous environment, where the effects of inertia are negligible. Nevertheless, by oscillating in a periodic, time-irreversible manner, the cilia can generate net currents within the fluid and thereby, effectively pump the food particles towards the feeding animals. The velocity of water propulsion depends on cilia length, beat frequency, pattern of beating, the arrangement of the cilia and their co-ordination. Beating cilia influence a layer of water only two or three cilium lengths deep, with maximal velocity near the cilia tip [33]. Mayer et al. [34] developed numerical model of cilia-driven flow, simulating metachronal wave transporting the particle.

The behavior of these biological cilia provides a useful design concept for creating microfluidic devices where actuated "synthetic cilia" would regulate the movement of microscopic particles (e.g., biological cells or polymeric microcapsules) within the device. Inspired by the effectiveness of biological cilia, recently there has been a tremendous interest in designing artificial ciliated system that is suitable for microfluidic mixing and flow manipulation. Lack of efficient manufacturing techniques and effective actuation impede the

progress of artificial cilia in microfluidics for long. However, Evan et al. [35] have recently created a magnetic actuation technique for ciliated surfaces, based on high-aspect-ratio cantilevered micro- and nanorod arrays. This development triggered several investigation related to effect of actuated cilia on flow structure in microfluidics devices. Oh et al. [20] have developed a microfluidics mixer based on actuated cilia.

The development of microfluidic channels that encompass synthetic cilia is still in its infancy; nonetheless, recent experiments [36] demonstrated that actuated polymeric cilia are effective at pumping fluids within a prototypical device. In addition, very efficient mixing is obtained using specially designed geometrical cilia configurations in a micro-channel. Since the artificial cilia can be actively controlled using electrical signals, they have exciting applications in micro-fluidic devices. Baltussen et al. [37] studied effectiveness of actuated cilia as a micro-mixer exhaustively. Kieseok Oh et al. [38] developed a bio-mimetic microfluidic device that mimics the high compliance and the beating frequency of biological cilia in order to achieve bio-compatible manipulation of microfluidics. To facilitate the design of the next stage devices, there is a need for computational studies that not only pinpoint the parameter space where the synthetic cilia would be most efficient, but also bring to light new functions that these filaments could perform. To date, there have been few simulations of the motion of microscopic particles in the three-dimensional fluid flow that is generated by the beating of cilia. The potential functionality of synthetic filaments in the selective trapping of particles from the solution or the expulsion of trapped species remains unexplored. Similarly, the effectiveness of actuated cilia in transporting a particle along a ciliated surface has not been studied.

### 1.3. Scallop Theorem

The mechanism behind micro-flow created by actuated cilia is similar to swimming at low Re. Actuated cilia can be considered as tethered swimmers. According to scallop theorem [39], to create a non-zero time-averaged flow, a swimmer must bend in way that is not invariant under time-reversal. In other word, one cannot swim at low Reynolds numbers with self-retracing strokes. An analog of scallop theorem for pumping states that there is neither momentum nor angular momentum transfer in a pumping cycle that is self-retracing. At low Re, flow through a micro-channel is linear. This can be seen from the fact that $V_s dt$ is balanced by $-V_s dt$ when the path is retraced. So, to create a time-averaged flow by a deforming body such as a tethered cilium, it must not deform in a time-variant reciprocal manner. For a deformation to be time-irreversible, the swimming system must have multiple degrees of freedom. Since cilia are tethered to the wall, it performs cyclic motion. We need to have some asymmetry in the system that can be done by rotation, facilitated by multiple degrees of freedom.

As demonstrated in Figure 1, a body with two-degrees of freedom (α,β) performs cyclic motion. The body which has a shape shown by the solid line changes its shape to the dashed contour and then it changes back to its original shape. During this cyclic motion, it utilizes its multi-degree freedom for producing time-irreversible cyclic motion. As evident from figure 1, configuration S2 and S4 are not identical. So, the body is not performing time-invariant motion. This irreversibility is manifested by the rotation between state 1 (represented by solid blue line) and state 2 (represented by solid red line). This is enough to elude the scallop theorem. As momentum of the system is conserved, rotation of the body will create flow in the surrounding liquid.

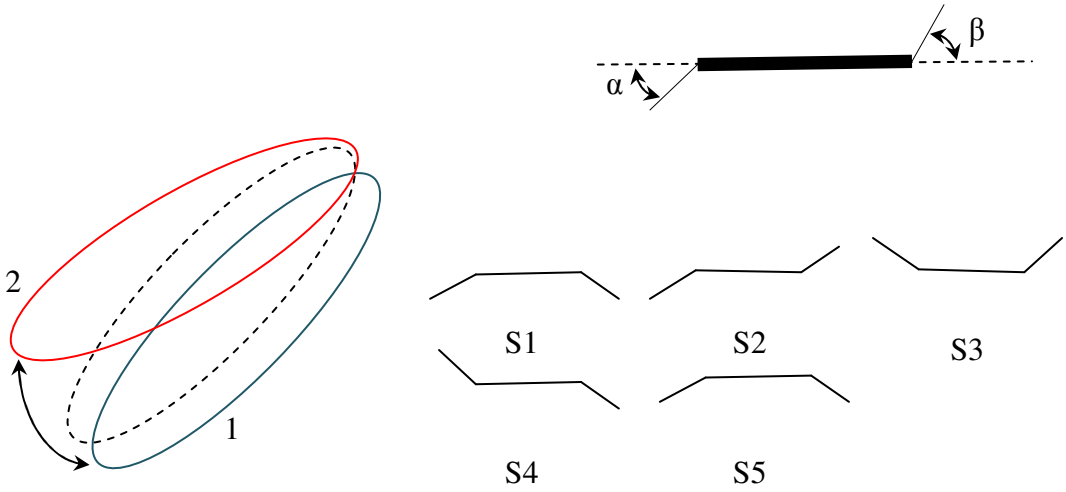


Figure 1: Non-reciprocal cyclic motion and resultant effect on fluid pumping

To create actuation that is not invariant under time-reversal, we can use oscillating elastic cilia, which have multiple (>2) degrees of freedom and can deform in such a manner that it need not have to retrace its trajectory. This justifies the choice of polymers for the material of artificial cilia. Unlike biological cilia, artificial cilia have identical forward and reverse strokes. The net transport in the layer of artificial cilia is due to secondary flow, generated by the non-recipetorial motion of elastic cilia.

### 1.4. Viscoelastic Coupling at Low Re Flow

Our system is governed by viscously over damped dynamics [40]. By numerical techniques, we couple elasticity theory and over-damped viscous hydrodynamics. Fluid flow in microfluidic devices is characterized by small length scale, result into low Reynolds number. At low Re, inertia is negligible compared to viscous effect. Since inertia is negligible, the motion is perfectly reversible in time. Time, in fact, makes no difference on flow pattern.

Assuming the surrounding fluid to be incompressible and its motion is governed by the Navier-Stokes equations:

$$\rho(\frac{\partial u_i}{\partial t} + u_j \frac{\partial u_i}{\partial x_j}) = \frac{\partial \tau_{ji}}{\partial x_i} + F_{ext}. \quad \textbf{(1)}$$

At low Re, in negligible inertia, it reduces to

$$\frac{\partial \tau_{ji}}{\partial x_i} = F_{ext}. \quad \textbf{(2)}$$

In elastohydrodynamic actuation, oscillating elastic bodies are used for triggering micro flows by time-varying external force, $A\cos(\omega t)$. This leads to bending in elastic cilia. The resultant flow field emerges due to the coupling between elastic force exerted on liquid by cilia and viscous drag force. The dynamics of elastic cilia in the limit of small deflection $y(x,t)$ is governed by the following 4th order partial differential equation:

$$y_t = -\bar{v} y_{xxxx}, \quad \textbf{(3)}$$

where $\bar{v}$ is the ratio of bending modulus and drag coefficient. Natural length of the system for frequency $\omega$, is $l(\omega) = (\frac{EI}{\omega\xi})^{0.25}$. To characterize the frequency in this overdamped viscous system, we use a non-dimensional number, called 'sperm number', $Sp = l/l(\omega)$. We therefore use the sperm number to characterize the motion of elastic cilia.

Frequency of biological cilia is in the range of 10-200Hz [41]. For our artificial cilia of length, $l = 40\mu m$, square cross-section with side length, $a = 4\mu m$, polymeric material elastic modulus, $E = 100KPa$, surrounded by water with viscosity $10^{-3} Pa.s$, and actuation frequency 10-200 $Hz$, the 'Sperm Number', $Sp$ of cilia is in the range of 3-5. In low $Sp$, cilia wiggle time-invariantly and unable to produce any time-averaged propelling effect. On the other hand, in large $Sp$, significant viscous damping suppresses cilia motion and again results a weak propelling effect. Within these two extremes, cilia dynamics and associated propulsion are

governed by interplay between elastic bending of cilia and viscous drag it experienced from surrounding fluid. In this range, we can expect effective propulsion from cilia.

As explained later, bending modes of elastic cilia oscillating at $Sp = 3$ and $Sp = 5$ are different. For $Sp = 3$, cilia exhibit the first mode of bending, whereas for $Sp = 5$ the bending is characterized by the second mode. As we will show, the difference in viscoelastic coupling between two these $Sp$ numbers leads to different directions of associated cilia-driven flow.

# CHAPTER 2

# PROBLEM DEFINITION

We use three-dimensional computer simulations to probe the utility of a ciliated surface to control the motion of microscopic solid particles within a microfluidic channel, where the fluid is characterized by a low Reynolds number (Re). Specifically, the problem addressed in this thesis is to identify design specifications for artificial cilia based microfluidics devices, those are capable of maneuvering a microscopic particle vertical to the channel wall, and transporting the particle parallel to the channel wall.

We model our system computationally, where the cilia are elastic filaments that are tethered to a solid wall and actuated by externally applied periodic forces. We introduce a neutrally buoyant, solid particle of radius $R$, which is sufficiently small (compared to the cilium length and inter-cilium distances) that the particle can move freely inside the ciliated layer. We assume that the micron-scale particle and cilia are sufficiently large, however, so that they are not affected by Brownian fluctuations.

As we show below, the actuated motion of these synthetic cilia can cause the particle to move perpendicular to the cilial layer. Furthermore, by changing the frequency of the applied force, we can regulate the direction of the particle's migration. In effect, this synthetic system mimics the ability of the marine suspension-feeders to manipulate particulates in their environment and can be utilized to facilitate either the deposition or removal of particles from substrates in microfluidic devices. In addition, we investigate the capability of actuated cilial layer to transport particles parallel to a substrate wall. In this case, the cilia are tethered at an

angle $45^0$ to the wall and actuated by externally applied forces. Similarly to the case of cilia perpendicular to the channel wall, we introduce a neutrally buoyant, solid particle that can move freely inside the ciliated layer, but not affected by Brownian fluctuations. As shown below for a given frequency and initial position of the particle, cilia can transport the particle by a considerable distance parallel to channel wall.

# CHAPTER 3

# METHODOLOGY

Our simulation box encompasses oscillating cilia and a suspended particle, which are immersed in a viscous fluid. To capture the complex fluid-structure interactions in this multi-component system, we employ a hybrid "LBM/LSM" approach [42-46], which integrates the lattice Boltzmann model (LBM) [47-48] for hydrodynamics and the lattice spring model (LSM) [49-50] for the micromechanics of elastic solids. Put succinctly, the LBM is an efficient solver for the Navier-Stokes equation. Via the LSM, we can fashion the cilia and the particle from a network of harmonic "springs", which connect nearest and next-nearest neighbor lattice nodes.

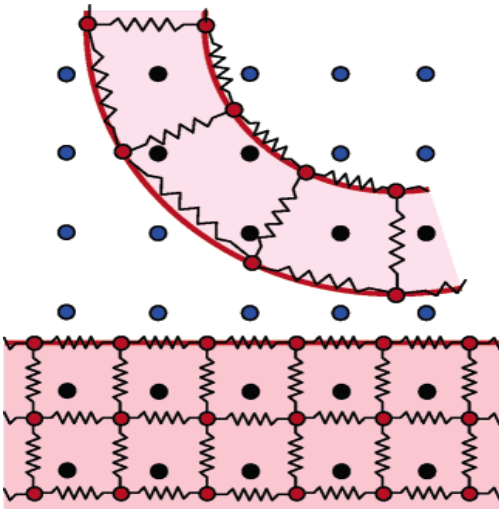

Figure 2: Schematic of computational system. The nodes that are connected by springs form the lattice spring lattice (for clarity, we omitted the diagonal springs that connect each node with all its next-nearest neighbors). The remaining nodes represent the lattice Boltzmann lattice (blue for fluid nodes and black for solid nodes). The solid lines are the solid-fluid interfaces.

### 3.1. Lattice Boltzmann Model

Lattice Boltzmann model is a lattice-based method for simulating hydrodynamic flows. The model is comprised of two processes. First is the propagation of fluid "particles" to neighboring lattice sites, and second being collisions between particles when they reach a site. The system is characterized by a single particle velocity distribution function, $n_i(r,t) \equiv n(r,c_i,t)$ describing local mass density of fluid particles with velocity $c_i$ at a lattice node at $r$ time $t$. Here, $c_i$, $r$, and $t$ are discrete variables, while the distribution function itself is a continuous variable. The hydrodynamic quantities, mass density, $\rho$; momentum density, $j = \rho u$; momentum flux, $\Pi$; are moments of the distribution function:

$$\rho = \Sigma_i n_i, j = \Sigma_i c_i n_i, \Pi = \Sigma_i c_i c_i n_i . \quad \textbf{(4)}$$

The distribution function varies with time in accordance with the discretized Boltzmann equation:

$$n_i(r + c_i \Delta t, t + \Delta t) = n_i(r,t) + \Delta[n(r,t)] . \quad \textbf{(5)}$$

Here, the collision operator $\Delta[n(r,t)]$ quantifies the change in distribution function, $n_i$ due to instantaneous collisions at the lattice nodes. A multi-relaxation time collision operator is employed for assigning independent values to the shear and bulk viscosities. This collision operator conserves mass and momentum. It also relaxes the momentum flux (or stress) toward local equilibrium. The velocity $c_i$ in the $i$-th direction is specified such that fluid particles take exactly one time step $\Delta t$ for propagating from one lattice site to the next.

A computationally efficient form for the collision operator can be modeled by linearizing about the local equilibrium $n^{eq}$ as:

$$\Delta_i(n) = \Delta_i(n^{eq}) + \Sigma_i L_{ij} n_j^{neq}, \quad \textbf{(6)}$$

where $L_{ij}$ are the matrix elements of the linearized collision operator, $n_j^{neq} = n_j - n_j^{neq}$ , and $\Delta_i(n^{eq}) = 0$ . The computational utility of lattice-Boltzmann models depends on the fact that only a small set of velocities are necessary to simulate the Navier–Stokes equations.

A particular lattice-Boltzmann model is defined by a set of velocities $c_i$ , an equilibrium distribution $n_i^{eq}$ , and the eigen-values of the collision operator. The population density associated with each velocity has a weight $a^{ci}$ that describes the fraction of particles with velocity $c_i$ in a system at rest; these weights depend only on the speed $c_i$ and are normalized so that their sum equals to unity. Note that the velocities $c_i$ are chosen such that all particles move from node to node simultaneously. For any cubic lattice,

$$\sum_i a^{c_i} c_i c_i = C_2 c^2 1; \quad \textbf{(7)}$$

where, $c_i = \Delta x / \Delta t$ , $\Delta x$ is the grid spacing, and $C_2$ is a numerical coefficient that depends on the choice of weights. However, in order for the viscous stresses to be independent of direction, the velocities must also satisfy the isotropy condition;

$$\sum_i a^{c_i} c_{i\alpha} c_{i\beta} C_{i\gamma} C_{i\delta} = C_4 c^4 \{\delta_{\alpha\beta}\delta_{\gamma\delta} + \delta_{\alpha\delta}\delta_{\gamma\beta} + \delta_{\alpha\gamma}\delta_{\beta\delta}\}. \quad \textbf{(8)}$$

In three dimensions, isotropy requires a multi-speed model; for example the 18-velocity model. This model employs the [100] and [110] directions of a simple cubic lattice, with twice the density of particles moving in [100] directions as in [110] directions; alternatively a 14-velocity model can be constructed from the [100] and [111] directions with a density ratio of 7:1.

The form of the equilibrium distribution is constrained by the moment conditions required to reproduce the inviscid (Euler) equations on large length scales and time scales. In particular, the second moment of the equilibrium distribution should be equal to the inviscid momentum flux $p\mathbf{1}+\rho uu$ **:**

$$\rho = \sum_i n_i^{eq}. \tag{9}$$

$$j = \sum_i n_i^{eq} c_i. \tag{10}$$

$$\prod^{eq} = \rho c_s{}^2 1 + \rho uu. \tag{11}$$

$$\sum_i n_i^{neq} = \sum_i n_i^{neq} c_i = 0 \tag{12}$$

The linearized collision operator must satisfy the following eigen-value equations;

$$\sum_i L_{ij} = 0, \sum_i c_i L_{ij} = 0, \sum_i \overline{c_i c_i} L_{ij} = \lambda \overline{c_j c_j}, \sum_i c_i^2 L_{ij} = \lambda_v c_j^2. \tag{13}$$

where $\overline{c_i c_i}$, indicates the traceless part of $c_i c_i$. The first two equations follow from conservation of mass and momentum, and the last two equations describe the isotropic relaxation of the stress tensor; the eigen-values $\lambda$ and $\lambda_v$ are related to the shear and bulk viscosities and lie in the range $-2 < \lambda < 0$. In general the eigen-values of these kinetic modes are set to $-1$, which both simplifies the simulation and ensures a rapid relaxation of the non-hydrodynamic modes.

The collision operator can be further simplified by taking a single eigen-value for both the viscous and kinetic modes. This exponential relaxation time (ERT) approximation, $\Delta_i = -n_i^{neq}/\tau$, has become the most popular form for the collision operator since it is simple and computationally efficient. However, the absence of a clear time scale separation between the kinetic and hydrodynamic modes can sometimes cause significant errors at solid-fluid boundaries.

The distribution function post-collision can be written as:

$$n_i^* = a^{c_i}\left(\rho + \frac{j.c_i}{c_s^2} + \frac{\left(\rho uu + \Pi^{neq_i^*}\right):\left(c_i c_i - c_s^2 1\right)}{2c_s^4}\right). \qquad \textbf{(14)}$$

The zero[th] ($\rho$) and first ($j=\rho u$) moments are the same as in the equilibrium distribution but the non-equilibrium second moment $\Pi^{neq}$ is modified by the collision process:

$$\Pi^{neq_i^*} = (1+\lambda)\overline{\Pi}^{neq} + \frac{1}{3}(1+\lambda_v)(\Pi^{neq}:1)1, \qquad \textbf{(15)}$$

where $\Pi^{neq} = \Pi - \Pi^{eq}$ ; The kinetic modes can also contribute to the post-collision distribution, but we choose the eigen-values of these modes to be $-1$, so that they have no effect on $n_i^*$ with $\lambda = \lambda_v = -1$ is equivalent to the ERT model with $\tau = 1$ for $\lambda < -1$, the kinetic modes relax more rapidly than the viscous modes, which is the proper limit for hydrodynamics.

### 3.2. Lattice Spring Model

The elastic and plastic response of the material is represented by an array of `springs' which occupy the nearest, and next nearest neighbor, bonds of a simple cubic lattice. The energy associated with a node *m* in the lattice is assumed to be of the form,

$$E_m = \frac{1}{2}\sum\nolimits_n (u_m - u_n).M_{mn}.(u_m - u_n). \qquad \textbf{(16)}$$

where the summation is over all the neighboring nodes, *n*, attached to *m* by a spring, $u_m$ is the displacement of node *m*, and $M_{mn}$ is a symmetric matrix which determines the elastic properties of the springs. It is shown in the subsequent parts of this section that this system of springs obeys, to first order, the equations of continuum elastic theory for isotropic elastic medium whose elastic constants can be determined in terms of the elements of the matrices $M_{mn}$. The harmonic form of the energy results in forces which are linearly dependent upon the

displacement of the nodes and the resulting set of sparse linear equations may be solved by a conjugate gradient method to find the equilibrium configuration which corresponds to no net force at each node. The matrices $M_{mn}$ associated with a bond can be varied to represent the material properties present in different phases within the same material, hence allowing heterogeneous systems to be simulated. Bonds which straddle two phases are assigned linearly interpolated values.

We assume that the matrix associated with the spring in the [100] direction is of the form

$$M_{[100]} = \begin{pmatrix} k_1 & 0 & 0 \\ 0 & c_1 & 0 \\ 0 & 0 & c_1 \end{pmatrix}, \qquad \textbf{(17)}$$

In this matrix, $k_1$ and $c_1$ correspond respectively to extensional and rotational force constants. We construct the matrices corresponding to the springs in the equivalent symmetry directions by a similarity transformation of the form

$$M' = R \cdot M \cdot R^T, \qquad \textbf{(18)}$$

where R is the rotation matrix which rotates a vector in the [100] direction into the required direction. In addition the matrices corresponding to the set of directions [110] have the force constants ($c_1$, $k_1$) replaced by ($k_2$ ,$c_2$).

Hence, for example, the matrix corresponding to the [110] direction is

$$M_{[110]} = \frac{1}{2}\begin{pmatrix} (k_2 + c_2) & (k_2 - c_2) & 0 \\ (k_2 - c_2) & (k_2 + c_2) & 0 \\ 0 & 0 & c_2 \end{pmatrix}. \qquad \textbf{(19)}$$

In the following analysis, we consider a homogeneous material in which only the force constants ($k_1$, $k_2$, $c_1$, $c_2$) are used. It is now shown how these constants may be chosen in order to recover an isotropic elastic medium.

In order to map the spring model onto the continuum equations we make the Taylor approximation:

$$u_m - u_n \approx u(x + (c_{mm})_{x,y} + (c_{mn})_y) - u(x, y) \approx (c_{mm} \bullet \nabla)u(x, y) + \frac{1}{2}(c_{mm} \bullet \nabla)^2 u(x, y), \textbf{(20)}$$

where, u(*x, y*) is the vector displacement field of a two dimensional continuum material and $c_{mn}$ are the bond vectors (*not* unit vectors). We may use this expansion in the expression $F_m = \sum_n M.(u_m - u_n)$ for the force on node *m* and derive the form of the Lame equations for the spring model. Alternatively an expression for the energy density can be derived using the Taylor approximation in the energy $E_m$ given by equation. If we equate coefficients in these equations with those for the elastic continuum and assume the primitive cell of the simple cubic lattice has unit side, we find the following relationships between the elastic constants of the continuum and spring models

$$b_1 = \frac{1}{2}(k_1 + 2k_2 + 2c_2), \quad \textbf{(21)}$$

$$b_2 = k_2 - c_2, \quad \textbf{(22)}$$

$$b_3 = 2k_2 + c_1 + 2c_2, \quad \textbf{(23)}$$

$$d_1 = c_1 + 4c_2. \quad \textbf{(24)}$$

It is important to note that although the term $d_1$ associated with the antisymmetric contribution to the free energy does not affect the elastic constants, it is essential for the term to be included if the mapping onto the continuum equations using the free energy expression and the Lame equations are to be consistent. In order for the spring model to become isotropic, we require $2b_1 = b_2 + b_3$ and for simplicity we choose and $k_2 = k_1$ and $c_2 = c_1$ and hence the spring model has the following properties:

$$M_{[100]} = \begin{pmatrix} k & 0 \\ 0 & c \end{pmatrix}, \qquad M_{[110]} = \frac{1}{2}\begin{pmatrix} k+c & K-c \\ k-c & k+c \end{pmatrix}, \tag{25}$$

$$\lambda = (k-c), \qquad \mu = \frac{1}{2}(2k+3c). \tag{26}$$

and hence,

$$E = \frac{5k(2k+3c)}{(4k+c)}, \qquad v = \frac{k-c}{c+4k}, \qquad K = \frac{3\lambda+2\mu}{3} = \frac{5k}{3}. \tag{27}$$

where $K$ is the bulk modulus. Furthermore, in our simulations we set $c = 0$ leading to $\nu = 0.25$.

In order to calculate the dynamics of an elastic solid, we assign a mass $M_i$ to each LS node at position $\mathbf{r}_i$ and integrate Newton's equation of motion, $\mathbf{F}(\mathbf{r}_i) = M_i\left(d^2\mathbf{r}_i/dt^2\right)$, where $\mathbf{F}$ is the total force acting on the node. Specifically, $\mathbf{F}$ consists of the force due to the interconnecting springs and the force exerted by the fluid on the solid at the solid-fluid boundary. The velocity Verlet algorithm is used to integrate this equation of motion.

### 3.3. Solid-Fluid Boundary Condition

To capture the interactions between the solids and fluids, lattice spring nodes that are situated at the solid-fluid interface must impose velocities on the surrounding fluids through boundary conditions and, in turn, experience forces due to the fluid pressure and viscous stresses. Put concisely, the simulation precedes through the sequential update of both the lattice spring and the lattice Boltzmann systems. The LSM system is updated by first calculating the forces that are acting on the LSM nodes, due to the LSM springs and the surrounding solvent. New positions, velocities, and accelerations of the LSM nodes are then calculated using the Verlet algorithm. In updating the LBM system, we first establish LBM links intersect the solid/fluid interface. We then obtain the velocities at these points of intersection from neighboring LSM nodes. Next, we

propagate the distribution function by streaming fluid particles to their neighboring nodes whenever these nodes are in the fluid domain, and otherwise, we apply the appropriate boundary condition (described below).

Finally, we modify the distribution functions at the LBM nodes to account for the collision step. We then repeat the entire cycle.

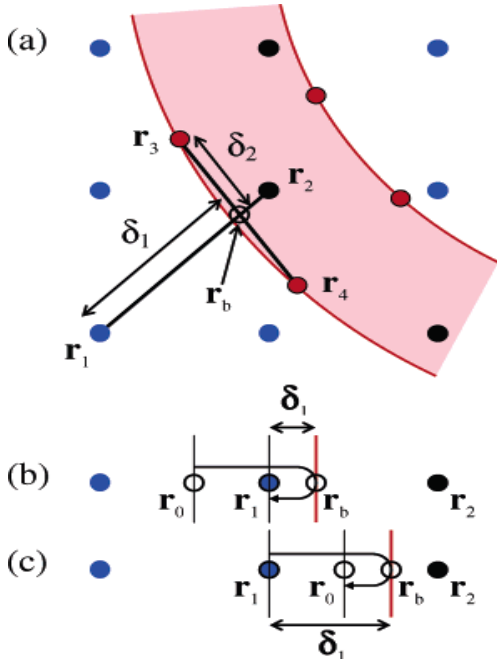


Figure 3: Implementation of solid-fluid boundary conditions

In our current implementation, fluid particles that are moving on a link that intersects the solid-fluid interface are bounced back into the fluid phase at the intersection point (or boundary node) $\mathbf{r}_b$. Here, $\delta_1 = |r_1 - r_b|\|r_1 - r_2|^{-1}$ , with $\mathbf{r}_1$ being the fluid node at which the fluid particles originate and $r_2 = r_1 + c_i \Delta t,$ being the neighboring solid node in the direction of the fluid particles' motion. For, $\delta_1 = \frac{1}{2},$ these particles will arrive back at node $\mathbf{r}_1$ after precisely one time step with a velocity that is opposite in direction to their original motion. This situation represents

the well known link bounce-back rule. However, for $\delta_1 \neq \frac{1}{2}$, fluid particles will end up at positions that do not coincide with a regular lattice node, and some sort of interpolation is needed [51-52].

First we consider an interface that is stationary. For $\delta_1 < (1/2)$, we obtain post-collision distribution function, $f_i^*(r_0,t)$ by linear interpolation between $f_i^*(r_1 - c_i\Delta t,t)$ and $f_i^*(r_1,t)$. After travelling for one time step and being reflected at the boundary node, the interpolated postcollision distribution function at $r_0$ will end up precisely at the node $r_1$ with velocity in the opposite direction (figure 2 (b)). Hence [22]

$$f_k(r_1,t+\Delta t) = f_i^*(r_0,t) = (2\delta_1 - 1)f_k^*(r_1 - c_1\Delta t,t) + 2\delta_1 f_i^*(r_1,t). \quad \textbf{(28)}$$

When $\delta_1 > 1/2$, we calculate a new distribution after it is bounced from the solid as follows,

$$\begin{aligned} f_k(\mathbf{r}_1,t+\Delta t) &= \frac{2\delta_1 - 1}{2\delta_1} f_k(r_1 - c_i\Delta t,t+\Delta t) + \frac{1}{2\delta_1} f_k(r_0,t+\Delta t) \\ &= \frac{2\delta_1 - 1}{2\delta_1} f_k^*(\mathbf{r}_1,t) + \frac{1}{2\delta_1} f_i^*(\mathbf{r}_1,t). \end{aligned} \quad \textbf{(29)}$$

Here, the subscript $k$ stands for fluid particles with a velocity in the opposite direction of the incoming particles, i.e. $\mathbf{c}_k = -\mathbf{c}_i$, and $a^{c_i} = 1/18$ for the orthogonal directions and $1/36$ for the diagonal links. we propagate the fluid particles at node $\mathbf{r}_1$, such that they end up at the position $\mathbf{r}_0$, i.e., $f_k(\mathbf{r}_0,t + ¢t)$ ) $fi^*(\mathbf{r}1,t)$ (see Figure 2c). We then obtain $f_k(\mathbf{r}1,t + ¢t)$ by linear interpolation between $f_k(\mathbf{r}_1 - \mathbf{c}_i\Delta t, t + \Delta t)$ and $f_k(\mathbf{r}_0,t + \Delta t)$ (figure 2 (c)).

For a moving interface, we have to account for the velocity, $u_b$ of solid material at the intersection point $r_b$. This leads to additional terms in equation (IV-25) and (IV-26) that are proportional to the component of the velocity $u_b$ in the direction of fluid particle velocity [22].

$$f_k(r_1,t+\Delta t)=f_i^*(r_0,t)=(2\delta_1-1)f_k^*(r_1-c_1\Delta t,t)+2\delta_1 f_i^*(r_1,t)-\frac{2\alpha_i}{c_f^2}\rho(r_1,t)c_i.u_b(r_b,t),$$
$$\delta_1<\frac{1}{2}. \tag{30}$$

$$f_k(\mathbf{r}_1,t+\Delta t)=\frac{2\delta_1-1}{2\delta_1}f_k^*(\mathbf{r}_1,t)+\frac{1}{2\delta_1}f_i^*(\mathbf{r}_1,t)-\frac{\alpha_i}{\delta_1 c_f^2}\rho(r_1,t)c_i.u_b(r_b,t),$$
$$\delta_1\geq\frac{1}{2}. \tag{31}$$

Here $\alpha_i=1/18$ for the orthogonal direction and 1/36 for the diagonal links. The velocity $u_b$ is obtained by interpolation between lattice spring nodes on either side of the interpolation points, i.e, $u_b(r_b,t)=(1-\delta_2)u(r_3,t)+\delta_2 u(r_4,t)$, with $\delta_2=|r_3-r_b|/|r_3-r_4|$ (see figure 2(a)). This implementation gives no-slip boundary condition with second order accuracy [42].

As a result of the bounce-back process, the fluid exerts a force on the solid. This force is taken to be equal to the rate of exchange in momentum that takes place as the fluid particles are reflected at the interface, i.e.,

$$\mathbf{F}_b(\mathbf{r}_b,t+\tfrac{1}{2}\Delta t)=\{[f_i^*(\mathbf{r}_1,t)-\alpha_i\rho(\mathbf{r}_1,t)]\mathbf{c}_i-[f_k(\mathbf{r}_1,t+\Delta t)-\alpha_i\rho(\mathbf{r}_1,t)]\mathbf{c}_k\}\Delta x^3\Delta t^{-1}. \tag{32}$$

The terms $\alpha_i\rho(\mathbf{r}_1,t)$ compensate for the ambient pressure, ensuring that the force on the interface is zero when the entire system is at rest. The force $\mathbf{F}_b$ is distributed as a load to the neighboring LSM nodes, while conserving the normal and tangential force on the interface:

$$F_b(r_3,t+\frac{1}{2}\Delta t)=(1-\delta_2)F_b(r_b,t+\frac{1}{2}\Delta t), \tag{33}$$

$$F_b(r_4,t+\frac{1}{2}\Delta t)=\delta_2 F_b(r_b,t+\frac{1}{2}\Delta t). \tag{34}$$

### 3.4. Model Validation

The coupled LBM/LSM model have been previously validated [42] in the limit of low Reynolds numbers, $\mathrm{Re} << 1$. Specifically, we verified the boundary conditions for a static non-compliant interface by simulating the drag force on a regular array of parallel cylinders, whose axes lie perpendicular to the mean flow direction and an array of regularly spaced spheres. We also calculated the drag force on a sphere placed in a middle of a periodical box. That arrangement represents an array of regularly spaced spheres that are constructed from two concentric layers of LSM nodes. The drag force was compared with previously published solutions and excellent agreement was found.

The dynamical coupling between the LBM and LSM models was validated by simulating the breathing modes of a fluid-filled cylindrical shell in vacuum [42]. The results indicate that our coupled model captures the correct frequencies to within one percent of the theoretical prediction for a large range of shell stiffness values. Similarly, we have studied the breathing modes of spherical fluid-filled shells and found close agreement with corresponding analytical solutions.

Additionally, we calculated the drag force on a flat plate for finite values of the Reynolds number. In these two-dimensional simulations, a steady flow was imposed parallel to the rigid plate. The results are shown in Figure 4, where they are compared with the prediction of a theoretical model. For a wide range of Reynolds numbers, we find perfect agreement with the theory in terms of the friction coefficient $C_d$, providing confidence that our hybrid model can capture the flows for a wide range of Reynolds numbers.

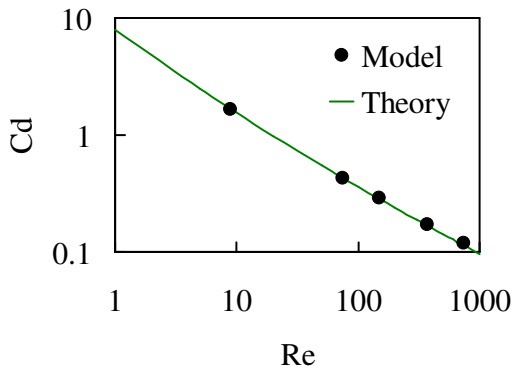


Figure 4 : Drag Coefficient vs Re

### 3.5. Dimensionless Parameters

The elasto-hydrodynamic behavior of beating cilia is normally analyzed in terms of the sperm number, $\mathrm{Sp}$, which characterizes the relative importance of the viscous force and the bending rigidity of oscillating cilia [53]. In particular, $\mathrm{Sp} = L(\zeta\omega/EI)^{0.25}$, where $\zeta = 4\pi\nu\rho$ is the viscous drag coefficient, $\omega = 2\pi f$ is the angular velocity of the driving force, and $EI$ is the bending rigidity of the cilium. In our simulations, we set the fluid density $\rho = 1$ and kinematic viscosity $\nu = 1/6$ (in LB units), and vary $f$ to alter the magnitude of $\mathrm{Sp}$. When $\mathrm{Sp}$ is relatively large, the dominant viscous effects suppress the wiggling of the elastic cilia, and consequently, no net fluid flow is generated. For relatively small $\mathrm{Sp}$, the dynamic shape of the cilium is governed by its elasticity, leading to time-reversible oscillations that are unable to generate net flows at low Re. It is only for intermediate values of $\mathrm{Sp}$, where the effects of cilium elasticity and fluid viscosity are of comparable magnitudes, that a coupling between elastic filaments and viscous fluid permits transport in the low Re environment.

Each cilium is driven by an oscillatory force that is applied to its free end. This sinusoidal force, which sets the entire system into periodic motion, is directed along the $x$-axis and has dimensionless amplitude $A = \frac{1}{3} aL^2 / EI$ and a frequency $f$. Here, $a$ is the force amplitude, and $I = b^4/12$ is the cilium's moment of inertia. In the ensuing simulations, we set $A = 1$, for studying the particle deposition discussed in the next Chapter, and $A$=5, for particle transport by tilted cilia described in Chapter 5.

### 3.6. Comparison with Experimental Parameters

When it comes to synthetic systems, a broad range of polymeric materials can be used to manufacture artificial cilia with sperm numbers in the range of interest. For example, let us consider a cilium that is $10\mu$m in length and $1\mu$m in diameter oscillating in water with a frequency of about 10 Hz (which corresponds to biologically relevant frequencies). For such cilia, a sperm number in the range from 1 to 10 can be obtained with polymers having a modulus of about $20\text{Pa} - 200\text{kPa}$, which is in the range of experimentally realistic values. Gueron et al. [54] explored different physical quantities related to biological cilia. In our model, we use radius of the particle as an independent parameter. We choose density and elastic constant equal to 1, and kinematic viscosity 1/6 based on our simulation scheme. We compared the values of Sp between our model and biological cilia, shown in table (1). We find that values of Sp used in our computational model are comparable to the values typical for biological cilia. We therefore expect similar functionality from our model.

**Table 1: Comparison between a biological system and the computational model, where radius of particle,** $R = 10 L.B.unit$

| Parameter | Biological System | Computational Model |
|---|---|---|
| $L$ | $12 \mu m$ | $4R$ |
| $a$ | $0.1 \mu m$ | $0.4R$ |
| $f$ | $28 beats/s$ | ---------- |
| $F$ | $10^{-12} N$ | $0.03R^2$ |
| $E_b$ | $25 \times 10^{-24} N/m^2$ | 1 |
| $\mu$ | $0.001 Kg/(ms)$ | $1/6$ |
| Sp | 6.5 | 3-5 |

### 3.7. Modeling Elastic Cilia

We construct each cilium from cubic elementary LSM units to form an elastic cantilever beam, which has a length of $L = 4R$, and a width of $b = 0.1L$. The inter-cilium separation is $B = 3R$. Given that $k$ is the spring constant of the interconnecting harmonic springs, the Young's modulus of the cilium is $E = 5k/2\Delta x_{\mathrm{LS}}$ and the solid density is $\rho_s = M/\Delta x_{\mathrm{LS}}^3$, where $\Delta x_{\mathrm{LS}} = 4/3$ is the spacing between the LS nodes. We set the Young's modulus $E = 1$ and density $\rho_s = 1$ (in LB units). This simple lattice model is restricted to a Poisson's ratio of $1/4$, although more complicated many-body interactions can be included to vary the ratio.

### 3.8. Modeling Particle

The particle's three-dimensional shell is constructed from two concentric layers of LS nodes. By using the Delaunay triangulation technique, we distribute nodes in a regular manner on each surface. These two concentric surfaces are separated by a distance that is equal to the average size of a triangular bond and are connected by springs between the nearest and next nearest neighbor nodes. The spring constant for springs located on the capsule surfaces and normal to the surfaces is $k$, while the diagonal springs have spring constants of $2/3k$. The particle has a radius of $R = 10$ lb units, with $N_0 = 642$ nodes on the surface, a shell thickness of $\Delta x_c \approx 1.4$, and density of $\rho_s = 1$. The Young's modulus of the shell is $E \approx 5/18$.

### 3.9. Cilia-Particle Overlap

To prevent overlap between the capsule and the cilium, we introduce the following Morse potential**:** $\phi(r) = \varepsilon(1 - \exp[-(r - r_0)/\kappa])^2$. Here, $\varepsilon$ and $\kappa$ characterize the respective strength and range of the interaction potential, and $r$ is the distance between a pair of LS nodes, where one node lies on the capsule's outer surface and the other lies at the cilium-fluid interface. The parameter $r_0 = 1.8$ is the equilibrium distance where the force due to the potential is zero. We fix $\varepsilon = \varepsilon_r = 0.005$ for the repulsive part of the potential ($r < r_0$), while for the attractive part ($r > r_0$), we set $\varepsilon = 0$ and $\kappa = 1$. We use all numbers in lb units.

# CHAPTER 4

# PARTICLE DEPOSITION

## 4.1. Computational Setup

We use four cilia and a particle in our simulation box as shown in Figure 5. The height of the simulation box is chosen to be $10R$ and the width equals $6R$. We apply periodic boundary conditions along the lateral directions. Each cilium is driven by an oscillatory force that is applied to its free end. This sinusoidal force, which sets the entire system into periodic motion, is directed along the $x$-axis and has dimensionless amplitude $A = 1$. The only independent parameter in our problem is particle radius, equal to 10 lb units.

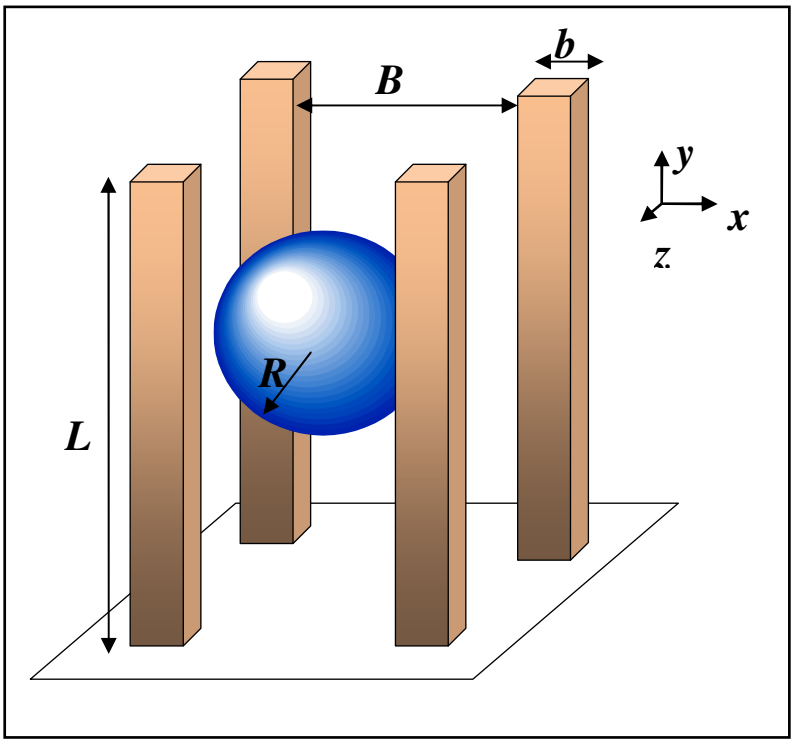


Figure 5: Schematic showing the three-dimensional arrangement of the cilia and the location of the spherical particle within the system.

### 4.2. Results and Discussion

Figure 6 shows snapshots from our simulations that illustrate the time-varying periodic movement of the compliant, synthetic cilia and solid particle. At the onset, we place a particle in the center (at $x = 0, z = 0$) between four initially quiescent cilia. We then apply the periodic, horizontal force, which drives the cilia to bend back and forth in the $x - y$ plane and thereby induce the movement of the fluid. The viscous fluid, in turn, imposes a periodic drag on the suspended particle. As a result, the particle follows the oscillatory motion of the beating cilia.

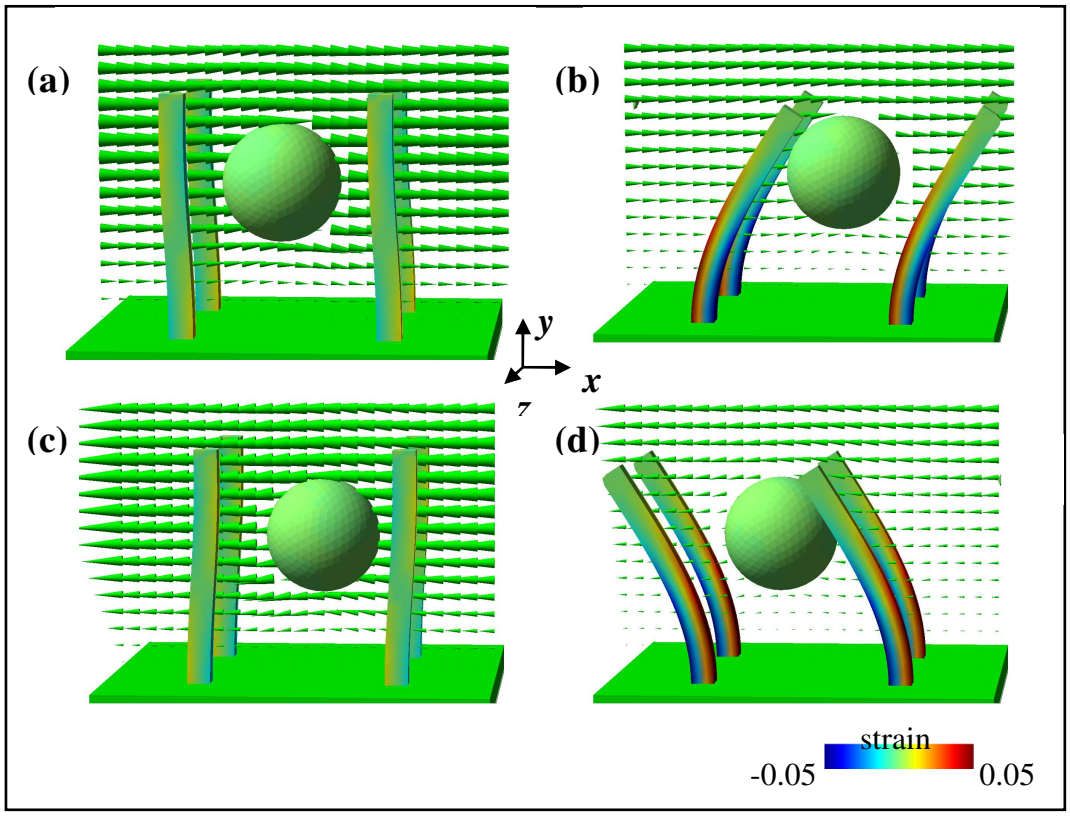


Figure 6: Snapshots from our simulations illustrating periodic oscillations of beating cilia and movement of solid particle for $\mathrm{Sp} = 3$. The colors on the cilium surface show the magnitude of material strain. The arrows indicate the direction and magnitude of fluid velocity at the plane $z = 0$. Panels (a), (b), (c), and (d) correspond to times $tf = 0$, 0.25, 0.5, and 0.75, respectively.

We investigate the effect of actuation frequencies on the dynamics of the particle motion. As mentioned previously, the actuation frequencies are characterized by $Sp = L\left(\frac{\xi\omega}{EI}\right)^{0.25}$. Specific trajectories for the particle's center of mass motion, scaled by the radius of the particle, are shown for $\mathrm{Sp} = 3$ and $\mathrm{Sp} = 5$ in Figure 7 (a) and (b), respectively. We observe that the particle follows an oscillatory trajectory. The particle oscillates in $x - z$ plane, i.e., in the plane parallel to force direction and normal to the channel wall. Interestingly, after a short initial transient behavior, the particles steadily migrate in a particular direction along the cilia (i.e., along the $y$ -direction). For lower frequency, characterized by $\mathrm{Sp} = 3$, the particle moves toward the bottom wall of the microchannel. When we increase the oscillatory frequency, characterized by $\mathrm{Sp} = 5$, the migration direction is reversed and the particle moves away from the surface. In other words, by simply changing the oscillating frequency, the actuated cilia can navigate solid particles toward or away from the channel wall, thereby controlling particle transport in vertical direction w.r.t. the channel wall. From Figure 7 (a), we observe that in 25 oscillations the particle migrates a distance equal to 0.6R. Thus, when $\mathrm{Sp} = 3$ for a particle of size $R = 10\mu m$, the transported distance is equal to $6\mu m$. From Figure 7 (b), we find that in 25 oscillations the particle migrates by distance equal to 0.015R, which corresponds to the transport of a particle of size $R = 10\mu m$ by a distance is equal to $0.15\mu m$. The slower transport at higher frequency can be explained by a higher viscous damping. Furthermore, larger amplitude of particle oscillations at lower frequency demonstrates the fact that, at lower Sp cilia wiggle more intensely.

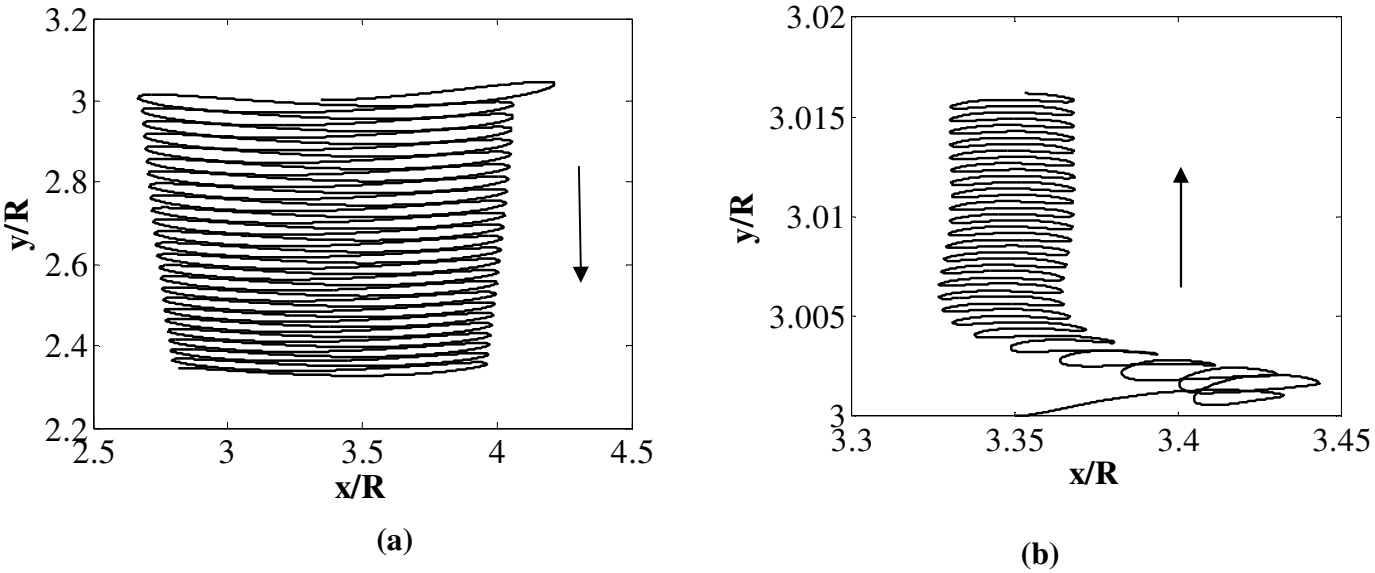


Figure 7: Trajectory of particles during 25 periods (a) low frequency characterized by Sp=3 and (b) high frequency characterized by Sp=5

We quantify the particle migration inside the ciliated layer by measuring $U$, the period averaged velocity normal to the channel wall. In these simulations, we allow the cilia to oscillate up to 25 periods to avoid the effect of the initial transient behavior. We calculate the period average velocity by measuring differences in displacements for successive periods and compute the average of the differences. The computed velocity, normalized by $\mathrm{Sp}^{-4}\, v/R$, is shown in Figure 8 as a function of particle distance from the channel wall for different $\mathrm{Sp}$. A positive velocity indicates that the particle is drifting away from the wall and vice versa.

We find that the drift direction indeed depends on the magnitude of $\mathrm{Sp}$. Moreover, for both $\mathrm{Sp} = 3$ and $\mathrm{Sp} = 5$, the velocities do not change sign inside the layer and even slightly above the cilia tips; this behavior indicates that actuated cilia can transport these particles in a

unidirectional manner all the way from the channel wall to the outer stream, where the effect of the beating cilia on the fluid flow eventually dissipates.

More specifically when $\mathrm{Sp} = 3$, the actuated cilia can actually trap a particle in the fluid above the layer and bring it into direct contact with the channel surface. Maximum normalized velocity, $URv^{-1}Sp^4$ reached by the particle at $\mathrm{Sp} = 3$ is equal to about 0.1, as shown in Figure 8. For a particle of size, $R = 10\mu m$ in water of kinematic viscosity $10^{-6} m^2 / s$, the velocity is equal to 0.0001 $ms^{-1}$. Negative velocity indicates the fact that, the particle is migrating towards the channel wall. Assuming average velocity is half of the maximum velocity, we can estimate that the actuated cilia will take 0.04s to deposit particle from outer layer to the channel wall. In this manner, the cilia can enhance the rate of deposition of suspended particles onto the underlying substrate.

Alternatively, cilia oscillating with $\mathrm{Sp} = 5$ can expel particles from the cilia layer and propel them into the outer fluid. In this way, actuated cilia can prevent particle accumulation on the surface. Maximum normalized velocity, $URv^{-1}Sp^4$ reached by the particle at $\mathrm{Sp} = 5$ is equal to about 0.1, as shown in Figure 8. For a particle of size, $R = 10\mu m$ in water of kinematic viscosity $10^{-6} m^2 / s$, the velocity $U$ is equal to 0.00016 $ms^{-1}$. Positive velocity indicates the fact that, the particle is migrating away from the channel wall. Assuming average velocity is half of the maximum velocity, we can estimate that the actuated cilia will take 0.25s to expel particles from the channel wall to outer layer. In this manner, the cilia can enhance the cleaning rate of suspended particles from the cilia layer.

We note that when the cilia are oscillating at $\mathrm{Sp} = 4$, the velocity fluctuates around zero and thus, there is little effect of the beating cilia on the net particle displacement relative to the

channel wall. At this point, it is prudent to note that for all Sp=3 and 5 maximum particle velocity is at $y \approx 0.8L$. Also, the particle velocity tends to be zero above cilia layer. These observations can be explained by the existence of secondary flows within cilial layer, as discussed further below.

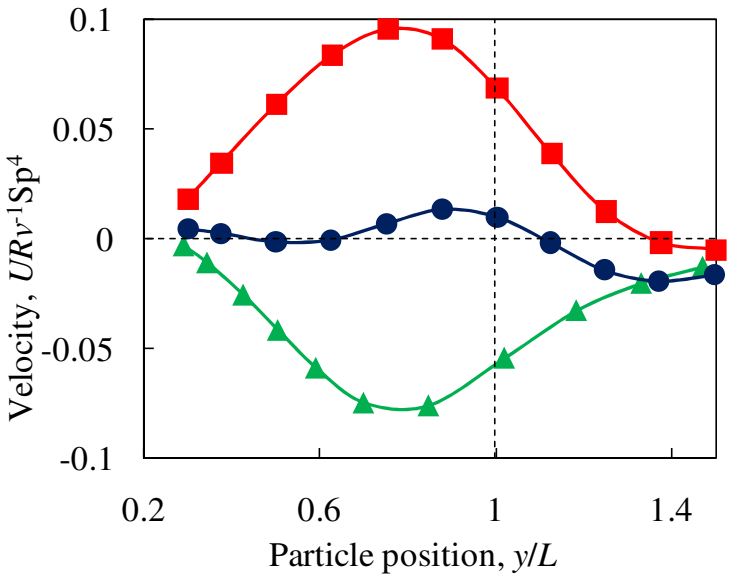


Figure 8: Velocity of particles as a function of distance from the bottom wall. The lines with triangles, circles, and squares show the particle velocities for Sp=3, Sp=4, and Sp=5, respectively

In the above simulations, we placed the particles along a line $[x=0, z=0]$ in the center of the simulation box and varied the particle's initial distance from the bottom wall. With the square arrangement of cilia considered here, these particle positions are symmetric relative to the beating filaments and, for this reason, allow particle migration only in the direction normal to the wall. To probe the generality of the observed behavior, it is instructive to break the planer symmetry and investigate the migration behavior of particles that are initially shifted in the $x$ and $z$ directions, i.e., placed along the lines $[x=\delta, z=0]$ and $[x=0, z=\delta]$. For both $\mathrm{Sp}=3$ and 5, we plot in Figure 9 (a) and (b) the velocities of particles displaced from the center of the

domain by distances of $\delta = c$ and $\delta = 0.5c$, where $c = 0.5(B + b)$. Note that $\delta = c$ are symmetry lines and, therefore, particles located on these lines can only migrate normal to the wall, whereas $\delta = 0.5c$ allows for migration both normal to the bottom surface and in-plane of the layer. For comparison purposes, we also plot in Figure 9 (a) and (b) the velocity for particles at $[x = 0, z = 0]$.

For $\mathrm{Sp} = 3$ (see Figure 9 (a)), particles along $[x = 0, z = 0]$ migrate down to the channel wall. When particles were shifted by $0.5c$ in the $z$-direction, i.e., normal to the plane of the cilium oscillation, the velocity of the shifted and non-shifted particles are almost identical. When we shifted the particles farther to $z = c$, the oscillating cilia come into contact with particles that are initially located near the cilium height. The latter contacts prevent the particles from moving into the cilial layer. In this case, we cannot measure the velocity since the cilia hit the particles during the first oscillation and push them to a position right above the layer, $y \approx 1.2L$. These situations are indicated by the discontinuity in the velocity profile in Figure 9 (a). As a result, the particles accumulate above the cilia. On the other hand, those particles that are initially relatively close to the wall migrate downwards and accumulate at $y \approx 0.5L$, where the velocity is zero. For particles shifted in the $x$-direction, i.e. parallel to the plane of cilia oscillations, and $\mathrm{Sp} = 3$, we found that for $x = c$, the particles move downwards only if they are initially closer than $y = 0.7L$ to the bottom wall. Otherwise, particles are repelled to the outer fluid, although with a velocity that is relatively slow compared to that at $x = 0$. For particles at $x = 0.5c$, the velocity is always downward, similar to the case for $x = 0$. Interestingly, the velocity at $x = 0.5c$ is approximately the average between the velocities at $x = 0$ and $c$. (Since the magnitude of the velocity at $x = c$ is smaller than that at $x = 0$, we expect that particles located between $x = 0$ and $c$ will mostly

move downwards.).In Figure 9 (b), we show how the migration velocity changes for $\mathrm{Sp}=5$ when particles are displaced either in the $x$ or $z$-direction. For this sperm number, particles in the middle of the domain migrate upwards from the solid wall. For $\delta=c$, the velocities are relatively slow and fluctuate around zero. The particles that are initially closer to the cilium tips exhibit positive velocities and migrate out of the layer, whereas particles closer to the channel wall concentrate near this surface. Again, we find that particles at $\delta=0.5c$ have velocities that are approximately an average of the velocities at $[x=0, z=0]$ and $\delta=c$, and always move away from the bottom wall. Hence, for $\mathrm{Sp}=5$, the actuated cilia will propel the particles away from the wall; except for a few cases where the particles are located between pairs of beating cilia (see Figure 9 (b)).

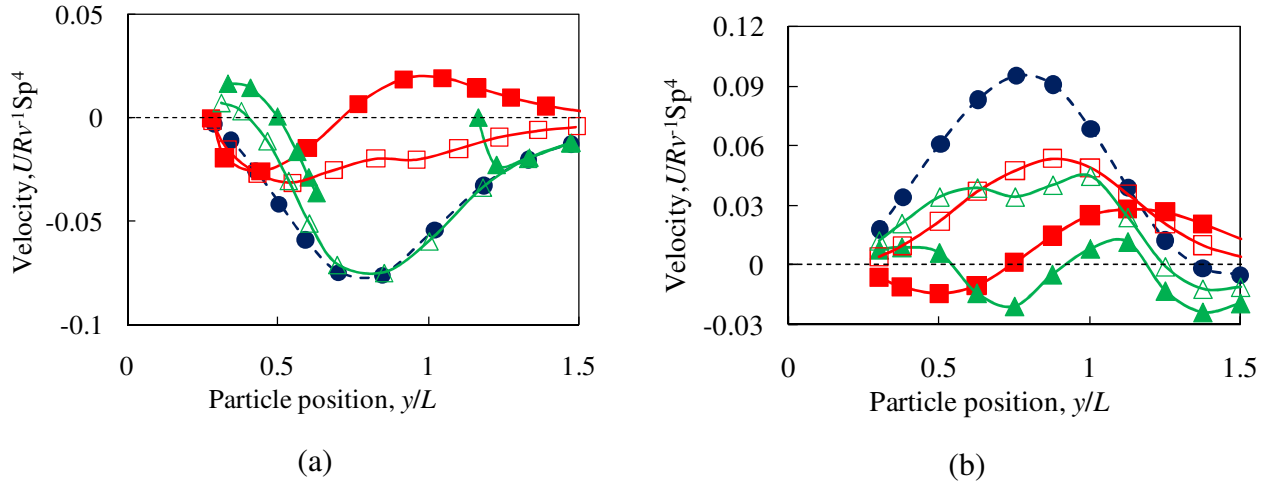


Figure 9: Velocity of particles as a function of distance from the bottom wall for (a) $\mathrm{Sp}=3$ and (b) $\mathrm{Sp}=5$. Particles with positive velocity move away from the wall. The dashed lines with filled circles indicate the velocity for particles located at the middle between oscillating cilia $x=0$ and $z=0$. The lines with the empty and filled squares indicate particles shifted to $x=0.5c$ and $x=c$, respectively. The lines with the empty and filled triangles indicate particles at $z=0.5c$ and $z=c$, respectively.

To gain insight into the effects that contribute to the controllable migration of the particle with changes in $Sp$, we examined the bending patterns for an individual cilium at both $Sp = 3$ and 5 as shown in Figure 10 (a) and (b). It reveals that indeed the cilium exhibit different dynamical behavior at these different $Sp$. In particular, at $Sp = 3$, the cilium makes extensive excursions in both the forward and backward motion. At the higher $Sp$, however, the effect of viscous damping is more pronounced and the cilium makes smaller deviations in the lateral direction. Similar dynamic behavior was previously observed for cilia that were tilted with respect to the substrate and were actuated by a periodic force. In the latter case, by changing $Sp$ (by altering the driving frequency $f$), one could switch the direction of the net flow within the microchannel [34]. Thus, it is clear that changes in $Sp$ affect not only the oscillatory behavior of the cilia, but also the fluid flow within the system.

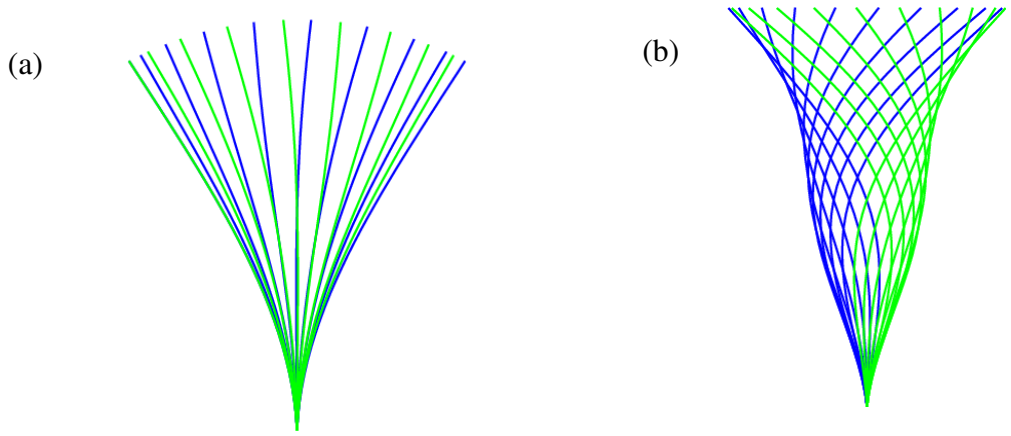


Figure 10: Cilium deformation during one beat cycle for (a) $Sp = 3$ and (b) $Sp = 5$. The blue lines show cilia when the force is directed to the right and the green lines show cilia when the force is directed to the left. For $Sp = 5$, the horizontal deflection is magnified tenfold for clarity.

In the current problem of particle deposition, the cilia are tethered normal to the solid surface and oscillation is symmetrical w.r.t. the normal of channel wall, therefore, no net flow is generated. Our simulations indicate, however, that the undulating filaments induce circulatory

secondary flows in the liquid and that the direction of these flows is controlled by the mode of filament deformation. To explore this effect, we introduced size-less tracer particles into the fluid and measured the flow velocities inside the cilia layer. As seen in Figure 11, where we plot the period averaged tracer velocities, the direction of flow circulation indeed depends on the magnitude of the sperm number. Specifically for velocities in the mid-plane between the actuated cilia, the flow is directed downwards when $\mathrm{Sp} = 3$ and upwards for $\mathrm{Sp} = 5$. These flow patterns agree with the directions of motion for the solid particles shown in Figures 9 (a) and (b). We note that the fluid continuity implies that the averaged fluid flow near a cilium surface and in the gap between cilia have opposite directions. For the relatively large particles considered here, however, the spheres remain in the middle between oscillating cilia and thus, follow the fluid flow arising in this location. This behavior, in turn, results in the observed unidirectional migration of the particles in the ciliated layer.

It is interesting to note that particle migration direction strictly follows secondary flow field direction. It demonstrates the negligible inertial effect on particle motion, typical of an overdamped highly viscous fluidic system.

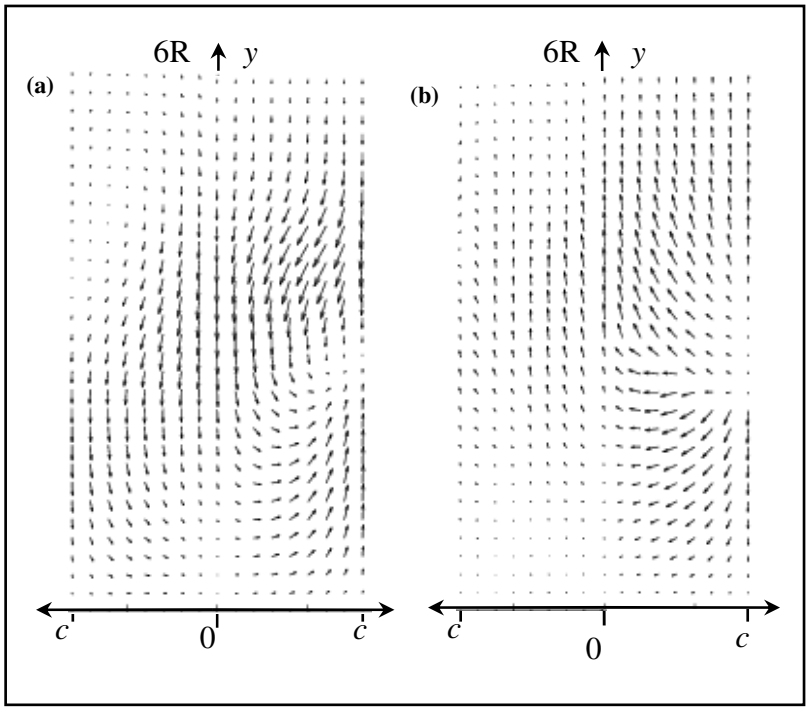


Figure 11: Hydrodynamic flow field in the middle between the cilia for (a) $\mathrm{Sp}=3$ and (b) $\mathrm{Sp}=5$. The velocities have been averaged over one period. The left and right parts of the plot represent the flow fields in $x-y$ and $z-y$ planes.

### 4.3. Validation and Closure

At this point of discussion, it is prudent to estimate the possible effect of gravity on particle motion and explore validity of our assumption of neutrally buoyant particles considered in our simulations. Terminal velocity of a particle in creeping flow is governed by the following equation,

$$V_t = \frac{gd^2}{18\mu}(\rho_s - \rho). \tag{35}$$

For a polymer particle with density $1330 kg/m^3$, suspended in water of dynamic viscosity $10^{-3} Pa.s$ and density $1000 kg/m^3$, terminal velocity is on the order of $10^{-10} m/s$. In our

simulation, maximum velocity of a spherical particle at $Sp = 5$ , is in the order of $10^{-5} m/s$ . So, we can safely neglect any effects due to buoyancy.

We can also calculate the terminal velocity of a bubble in a typical microfluidic device based on Equation (35). Typical bubble velocity is in the order of $10^{-6} m/s$ . Again, comparing to the particle velocity which is of the order of $10^{-5} m/s$ the bubble motion is significantly slower. Re .Therefore, we can claim even in the presence of air bubble, actuated particle can propel particles. Since the developed technique is independent of the presence of air bubble, the encapsulation of microfluidic devices utilizing the technique would not be an essential consideration. This is advantageous for fabricating a robust microfluidic device.

To estimate the effectiveness of oscillating synthetic cilia compared to diffusion velocity of at low Reynolds number, we calculate the diffusive rate for a microscopic particle in microfluidic devices. To this end we use the Einstein-Stokes equation

$$D = \frac{K_B T}{6\pi\mu r}, \tag{36}$$

Where the Boltzmann constant, $k_B = 1.38 \times 10^{-23} J/K$ . For a microscopic particle of radius, $r \sim 10^{-5} m$ at temperature $T = 300K$ , the diffusion rate in water is of the order of $10^{-12} m^2/s$ . Clearly, the Brownian diffusion does not have any significant effect on the particles considered in our studies.

To sum up, we have designed a technique for microscopic particle control in microfluidic devices. We have computationally demonstrated that by utilizing the technique, microscopic particle can be maneuver normal to the microfluidic channel wall at the rate much higher than diffusion that qualify our design to be a potential particle control technique in microfluidic

device. We have also quantified the effect of presence of air bubble and gravity and from that; we can safely conclude that the developed technique is robust to the presence of air bubble and the bouncy effect.

# CHAPTER 5

# PARTICLE TRANSPORT

## 5.1. Computational Setup

The computational setup we use to examine the transport of particles by inclined cilia is shown in Figure 12. In these studies, the height of the simulation box is $h = 6R$ and the width is $w = 6R$. Periodical boundary condition is imposed in the lateral directions. Each cilium is driven by an oscillatory force that is applied to its free end with dimensionless amplitude $A = 5$. The cilia are inclined at an angle $\alpha = 45^0$ with respect to the substrate. The outer radius of particle is $R = 10$ and cilium length is $L = 4R$.

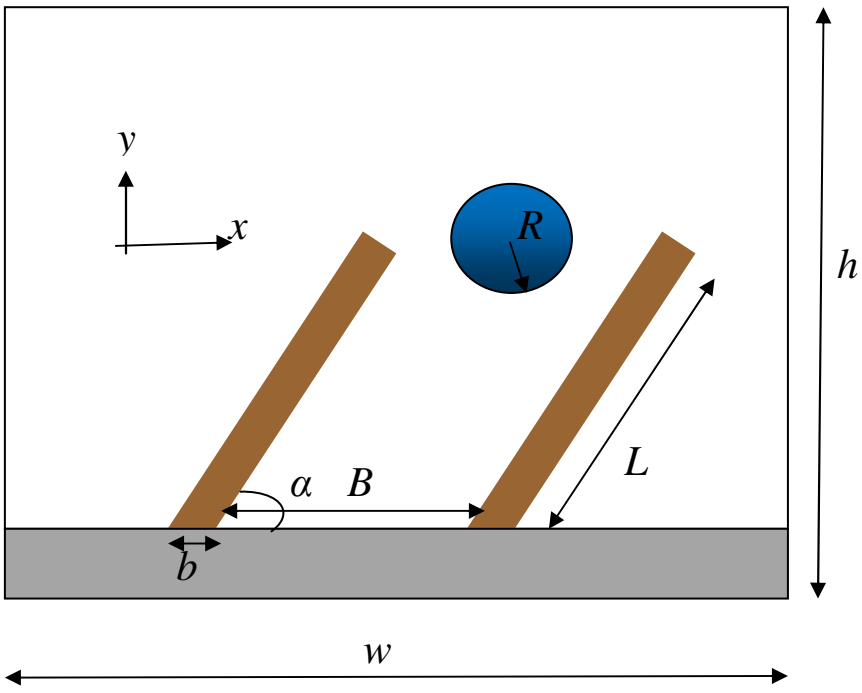


Figure 12: Schematic showing the three-dimensional arrangement of the cilia and the location of the spherical particle within the system.

## 5.2. Results and Discussions

Figure 13 shows snapshots from our simulations that illustrate the periodic movement of the compliant, synthetic cilia and solid particle. At the onset, we place a particle at a distance $4.5R$ from the bottom channel wall and in the center between two rows of inclined cilia. We then apply the periodic, horizontal force, which drives the cilia to bend back and forth in the $x-y$ plane and thereby induce the movement of the fluid. The viscous fluid, in turn, imposes a periodic drag on the suspended particle. As a result, the particle follows the oscillatory motion of the beating cilia.

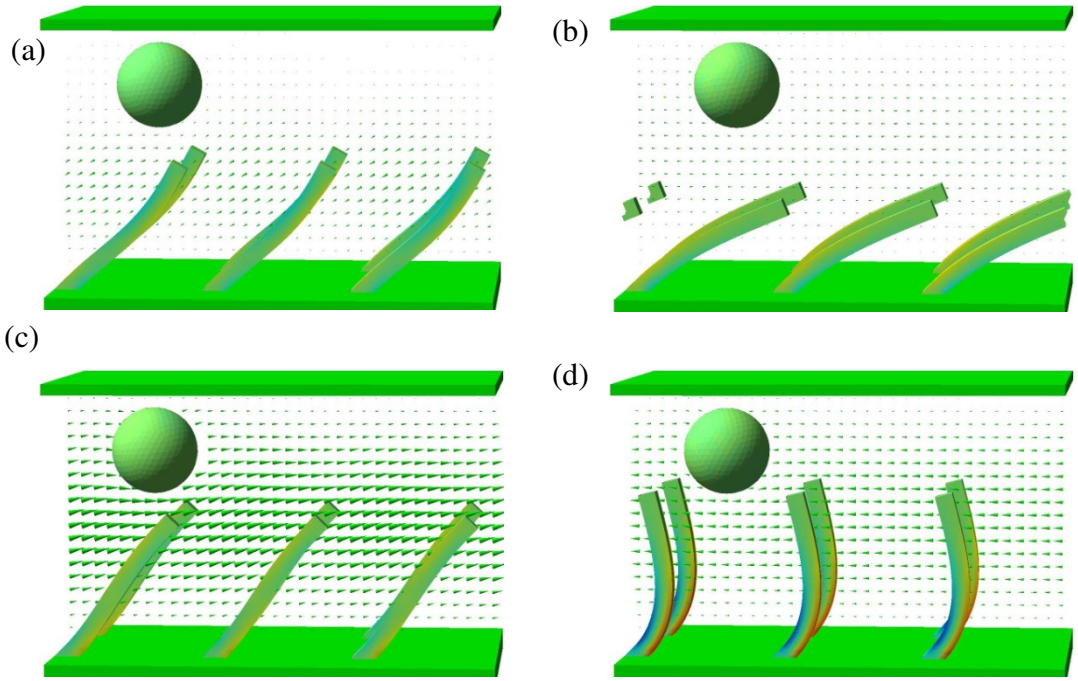


Figure 13: Snapshots from our simulations illustrating periodic oscillations of beating cilia and movement of solid particle for $\mathrm{Sp}=5$. The colors on the cilium surface show the magnitude of material strain. The arrows indicate the direction and magnitude of fluid velocity at the plane $z=0$. Panels (a), (b), (c), and (d) correspond to times $tf = 0.25,0.5,0.75,1$, respectively.

Specific trajectories for the particle's center of mass motion over 25 oscillation periods are shown for $\mathrm{Sp}=5$ and $\mathrm{Sp}=3$ in Figures 14 (a) and (b), respectively. While the particle follows oscillatory trajectories, it shows preferential drift direction. We find that at the distance $4.5R$ the particle exhibits maximum velocity along the ciliated layer. For both Sp, the particle migrates from left to right, along the cilia layer, however, for higher frequency the particle is transported by larger distance, equals to *3.5(B+b)* compared to $Sp=3,$ where displacement is marginal.

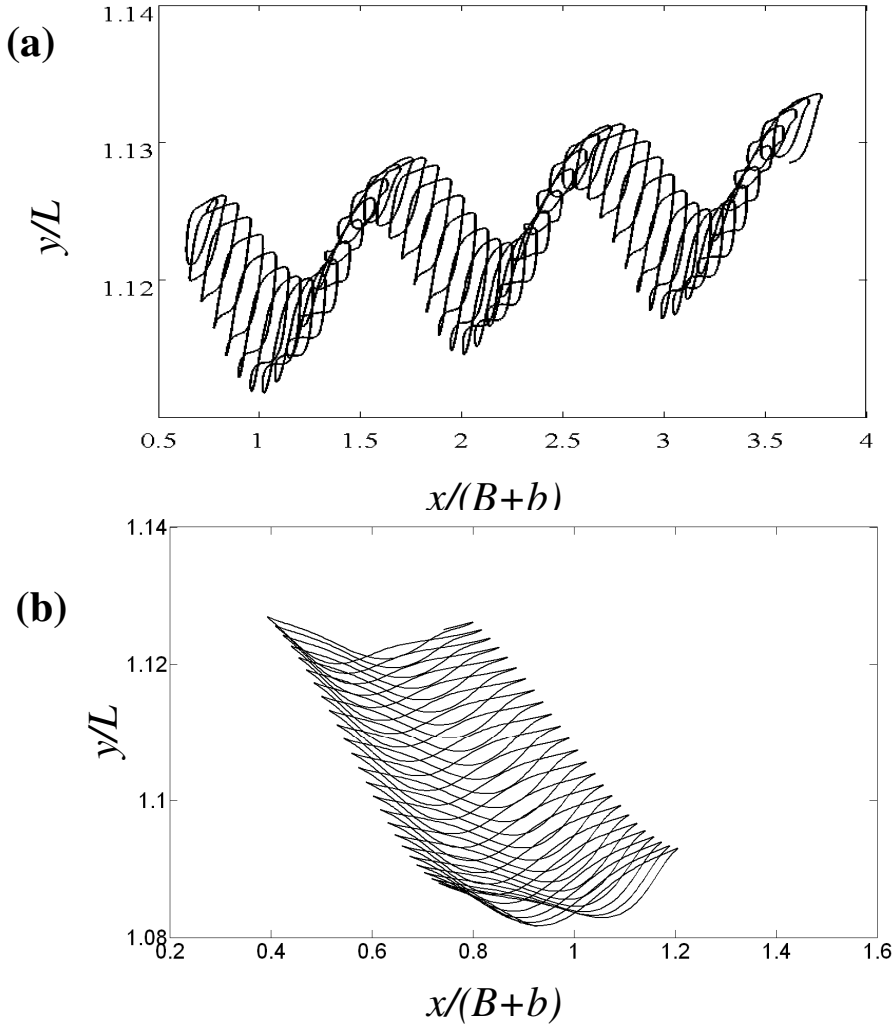


Figure 14: Trajectory of particles for 25 oscillations for particular frequencies characterized by (a) Sp=5 and (b) Sp=3

We quantify larger transport rate at $Sp = 5$ by computing period-averaged velocity along the ciliated layer. To this end, we average the velocity per period of the ciliated layer and normalize the particle velocity as follows $URv^{-1}Sp^4$. The normalized velocity is plotted in Figure 15 as a function of non-dimensional particle position, $x/(B+b)$. The particle velocity is positive everywhere, which indicates that actuated cilia transport particle in unidirectional manner along the ciliated layer and the transport direction is from left to right. We can associate this direction with the inclination direction of the quiescent cilia.

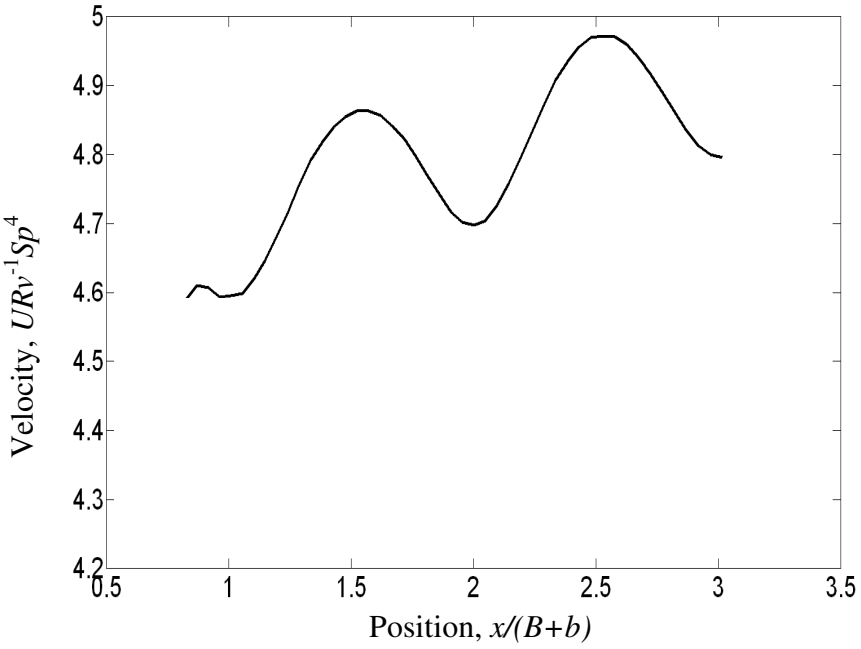


Figure 15: Velocity of particles as a function of distance along the ciliated layer for actuation frequency characterized by $Sp = 5$

From Figure 15, we can estimate average velocity, $URv^{-1}Sp^4$, which is equal to approximately 4.7. For a particle of size, $R = 10\mu m$ in water of kinematic viscosity, $v = 10^{-6} m^2/s$, the transport velocity, $U$ is about 0.002 ms$^{-1}$. With this velocity, transport time for a particle to traverse inter-cilia gap is about 0.015s.

### 5.3. Efficiency and Closure

To characterize the particle transport performance achieved by actuated cilia, we estimate mechanical efficiency, $\varepsilon$ by calculating the ratio between work required to transport particle in the viscous fluid during one oscillation period and work input required for driving oscillating cilia. We find in our simulation that the resulting efficiency is about $0.1\%$ .which is consistent with previously published results for pumping tilted cilia [45].

To sum up, we have designed a technique for transporting microscopic particles parallel to microfluidic channel wall.

## CONCLUSIONS

We find that actuated cilia can control the deposition of solid particles in microfluidic devices. For low frequency oscillations characterized by a sperm number of $\mathrm{Sp} = 3$, the cilia effectively draw particles from outside the layer and deposit particles to the underlying surface. For larger frequencies characterized by $\mathrm{Sp} = 5$, the cilia expel particles and therefore, can be used to clean the ciliated surface from foreign entities and inclusions.

In addition, we also find that actuated inclined cilia can regulate the transport velocity of solid particles along the ciliated layer. For higher frequency oscillations characterized by $Sp = 5$, the particle velocity along the ciliated layer is faster compared to lower frequency oscillation characterized by $Sp = 3$. Thus, we can use actuated cilia for transporting particles in microfluidic devices used for example in biomedical analysis.

It is noteworthy that on a very general level, our results show qualitative agreement with observations that the capture of food particles by certain suspension feeders is most effective for a finite range of ciliary beat frequencies. Furthermore, it is worth noting that behavior similar to what we find for $\mathrm{Sp} = 5$ has been observed experimentally in a microfluidic device that utilizes actuated synthetic cilia. In particular, the researchers detected an upward migration of suspended microscopic particles when the cilia are driven to beat at frequency of 65 Hz.

In addition to revealing new methods for manipulating particles for lab-on-a-chip applications, our studies can also provide some insight into factors that control the interactions between cilia in the respiratory tract and particulates such as dust or mucous. In particular, it has been reported that certain chemicals can increase the ciliary beat frequency and consequently, the cilia-driven particle transport within the trachea of mice. The physical mechanism for this

behavior is not completely understood. Ultimately, computational studies such as those described herein could reveal fundamental principles that contribute to the effective removal of unwanted particulates from the respiratory system.

## REFERENCES


[1] A. Manz, D.J. Harrison, E.M.J. Verpoorte, J.C. Fettinger, A. Paulus, H. Ludi, H.M. Widmer, Planar Chips Technology for Miniaturization and Integration of Separation Techniques into Monitoring Systems - Capillary Electrophoresis on a Chip, J Chromatogr, 593 (1992) 253-258.

[2] B. Bozic, V. Kralj-Iglic, S. Svetina, Coupling between vesicle shape and lateral distribution of mobile membrane inclusions, Phys. Rev. E, 73 (2006) 041915.

[3] D. Harrison, A. Van Den Berg, Micro total analysis systems' 98, Kluwer Academic, 1998.

[4] R. Anderson, H. Becker, A. Manz, Microsystem technology in chemistry and life science, Springer Berlin, 1998.

[5] J. Ramsey, S. Jacobson, M. Knapp, Microfabricated chemical measurement systems, Nature Medicine, 1 (1995) 1093-1095.

[6] L. Kricka, P. Wilding, Micromechanics and nanotechnology, Handbook of Clinical Automation, Robotics, and Optimization; Kost, GJ, Welsh, J., Eds.; John Wiley and Sons: New York, (1996).

[7] H. Becker, A. Manz, R. Anderson, Microsystem technology in chemistry and life science, Springer Verlag, 1998.

[8] R. Zengerie, S. Kluge, R. Richter, A bidirectional silicon micropump.

[9] S. Shoji, M. Esashi, Microflow devices and systems, J Micromech Microeng, 4 (1994) 157-171.

[10] F. Van de Pol, A Tbermopneumatic Micropump Based on Micro-ering Techniques, Sensors and Actuators, 21 (1990) 198-202.

[11] J. Folta, N. Raley, E. Hee, Design, fabrication and testing of a miniature peristaltic membranepump, in, 1992, pp. 186-189.

[12] J. Smits, Piezoelectric micropump with three valves working peristaltically, Sensors and Actuators, 21 (1990) 203-206.

[13] S. Bart, L. Tavrow, M. Mehregany, J. Lang, Microfabricated electrohydrodynamic pumps, Sens. Actuators A, 21 (1990) 193–197.

[14] G. Kovacs, Micromachined transducers sourcebook, Boston, 1998.

[15] M. Madou, Fundamentals of microfabrication: the science of miniaturization, CRC, 2002.

[16] C. Effenhauser, G. Bruin, A. Paulus, M. Ehrat, Integrated capillary electrophoresis on flexible silicone microdevices: analysis of DNA restriction fragments and detection of single DNA molecules on microchips, Anal. Chem, 69 (1997) 3451-3457.

[17] J. Jang, S. Lee, Theoretical and experimental study of MHD (magnetohydrodynamic) micropump, Sensors & Actuators: A. Physical, 80 (2000) 84-89.

[18] N. Pamme, Magnetism and microfluidics, Lab Chip, 6 (2006) 24-38.

[19] Y. Xiang, H. Bau, Complex magnetohydrodynamic low-Reynolds-number flows, Phys. Rev. E, 68 (2003) 16312.

[20] M. Madou, J. Zoval, G. Jia, H. Kido, J. Kim, N. Kim, Lab on a CD, (2006).

[21] D. Duffy, H. Gillis, J. Lin, N. Sheppard Jr, G. Kellogg, Microfabricated centrifugal microfluidic systems: characterization and multiple enzymatic assays, Anal. Chem, 71 (1999) 4669-4678.

[22] K. Sritharan, C. Strobl, M. Schneider, A. Wixforth, Z. Guttenberg, Acoustic mixing at low Reynold's numbers, Applied Physics Letters, 88 (2006) 054102.

[23] P. Marmottant, J. Raven, H. Gardeniers, J. Bomer, S. Hilgenfeldt, Microfluidics with ultrasound-driven bubbles, J. Fluid Mech., 568 (2006) 109-118.

[24] N. Riley, S TEADY S TREAMING, Annu. Rev. Fluid Mech., 33 (2001) 43-65.

[25] W. Lyne, Unsteady viscous flow over a wavy wall, J. Fluid Mech., 50 (2006) 33-48.

[26] D. Gaver, J. Grotberg, An experimental investigation of oscillating flow in a tapered channel, J. Fluid Mech., 172 (2006) 47-61.

[27] P. Hall, The linear development of Görtler vortices in growing boundary layers, J. Fluid Mech., 130 (2006) 41-58.

[28] N. Gilula, P. Satir, The ciliary necklace: a ciliary membrane specialization, Journal of Cell Biology, 53 (1972) 494.

[29] Y. Kim, R. Netz, Pumping fluids with periodically beating grafted elastic filaments, Phys. Rev. Lett., 96 (2006) 158101.

[30] S. Tamm, Ciliary motion in Paramecium: a scanning electron microscope study, Journal of Cell Biology, 55 (1972) 250.

[31] H. Riisgard, P. Larsen, Minireview: Ciliary Filter Feeding and Bio-Fluid Mechanics--Present Understanding and Unsolved Problems, Limnology and Oceanography, (2001) 882-891.

[32] D. Grunbaum, D. Eyre, A. Fogelson, Functional geometry of ciliated tentacular arrays in active suspension feeders, Journal of Experimental Biology, 201 (1998) 2575.

[33] M. Sleigh, Adaptations of ciliary systems for the propulsion of water and mucus, Comparative biochemistry and physiology. A, Comparative physiology, 94 (1989) 359.

[34] S. Mayer, Numerical simulation of flow fields and particle trajectories in ciliary suspension feeding, Bulletin of Mathematical Biology, 62 (2000) 1035-1059.

[35] B. Evans, A. Shields, R. Carroll, S. Washburn, M. Falvo, R. Superfine, Magnetically actuated nanorod arrays as biomimetic cilia, Nano Lett, 7 (2007) 1428-1434.

[36] J. den Toonder, F. Bos, D. Broer, L. Filippini, M. Gillies, J. de Goede, T. Mol, M. Reijme, W. Talen, H. Wilderbeek, Artificial cilia for active micro-fluidic mixing, Lab Chip, 8 (2008) 533-541.

[37] M. Baltussen, P. Anderson, F. Bos, J. Toonder, Inertial flow effects in a micro-mixer based on artificial cilia, Lab Chip, 9 (2009) 2326-2331.

[38] K. Oh, J. Chung, S. Devasia, J. Riley, Bio-mimetic silicone cilia for microfluidic manipulation, Lab Chip, 9 (2009) 1561-1566.

[39] E. Purcell, Life at low Reynolds number, Am. J. Phys, 45 (1977) 11.

[40] C. Wiggins, D. Riveline, A. Ott, R. Goldstein, Trapping and wiggling: Elastohydrodynamics of driven microfilaments, Biophys. J., 74 (1998) 1043-1060.

[41] S. Gueron, N. Liron, Ciliary motion modeling, and dynamic multicilia interactions, Biophys. J., 63 (1992) 1045-1058.

[42] A. Alexeev, R. Verberg, A. Balazs, Modeling the motion of microcapsules on compliant polymeric surfaces, Macromolecules, 38 (2005) 10244-10260.

[43] A. Alexeev, R. Verberg, A. Balazs, Patterned surfaces segregate compliant microcapsules, Langmuir, 23 (2007) 983-987.

[44] O. Usta, A. Alexeev, A. Balazs, Fork in the road: patterned surfaces direct microcapsules to make a decision, Langmuir, 23 (2007) 10887-10890.

[45] A. Alexeev, J. Yeomans, A. Balazs, Designing Synthetic, Pumping Cilia That Switch the Flow Direction in Microchannels, Langmuir, 24 (2008) 12102-12106.

[46] A. Alexeev, R. Verberg, A.C. Balazs, Patterned surfaces segregate compliant microcapsules, Langmuir, 23 (2007) 983-987.

[47] S. Succi, The lattice Boltzmann equation for fluid dynamics and beyond, Oxford University Press, USA, 2001.

[48] A. Ladd, J. Kinney, T. Breunig, Deformation and failure in cellular materials, Phys. Rev. E, 55 (1997) 3271-3275.

[49] G. Buxton, C. Care, D. Cleaver, A lattice spring model of heterogeneous materials with plasticity, Model. Simul. Mater. Sc., 9 (2001) 485-497.

[50] B. Delaunay, Sur la sph re vide, Bull. Acad. Sci. URSS, VII. Ser., 1934 (1934) 793-800.

[51] M. Bouzidi, M. Firdaouss, P. Lallemand, Momentum transfer of a lattice Boltzmann fluid with boundaries, Phys. Fluids, 13 (2001) 3452–3459.

[52] A. Koponen, D. Kandhai, E. Hellen, M. Alava, A. Hoekstra, M. Kataja, K. Niskanen, P. Sloot, J. Timonen, Permeability of three-dimensional random fiber webs, Phys. Rev. Lett., 80 (1998) 716-719.

[53] C. Lowe, Dynamics of filaments: modelling the dynamics of driven microfilaments, Philosophical Transactions of the Royal Society B: Biological Sciences, 358 (2003) 1543.

[54] S. Gueron, K. Levit-Gurevich, Computation of the internal forces in cilia: application to ciliary motion, the effects of viscosity, and cilia interactions, Biophys. J., 74 (1998) 1658-1676.